50th AIAA Aerospace Sciences Meeting including the New Horizons Forum and Aerospace Exposition
09 - 12 January 2012, Nashville, Tennessee

AIAA 2012-1206

Effects of Flexibility on the Aerodynamics of a Hovering Flexible Airfoil at Reynolds Number of 100 to 1000

Chang-kwon Kang*[1] and Wei Shyy†[1,2]

[1]Department of Aerospace Engineering, University of Michigan, Ann Arbor, MI, 48109

[2]Department of Mechanical Engineering, Hong Kong University of Science and Technology, Kowloon, Hong Kong

While biological flyers often display deformed wing structures, the effects of flexibility on the flapping wing aerodynamics remain inadequately understood. We investigate the lift generation and phase dynamics of a flapping flexible wing in hover, between Reynolds number of 100 and 1000 corresponding to small insects, using fully coupled Navier-Stokes equation and linear beam model. The γ scaling, which we recently reported relating the wing tip-deformation to the aerodynamic performance with low flapping-to-natural frequency ratio, is revised to account for wider frequency ratios. The lift averaged over a flapping cycle normalized by effective stiffness scales with the non-dimensional wing tip deformation and the power input scales with the phase lag introduced by the flexibility. It is shown that the phase lag between the prescribed plunging motion and the passive pitch can be varied by adjusting the frequency ratios, capable of producing advanced, synchronized, or delayed rotation modes. Whereas it is widely known that the advanced rotation yields the highest lifts for the rigid wing cases, the highest lift and the optimal efficiency are observed when the motion is in synchronized rotation mode, because the pitch angle is maximal at the midstroke. The main characteristics of the aerodynamic performance remain the same for the whole Reynolds number range considered.

Nomenclature

c	= chord	[m]
C_F	= coefficient of force deforming the wing, $F/(0.5\rho_f U^2_{ref} c)$	[1]
C_L	= lift coefficient, $-F_y/(0.5\rho_f U^2_{ref} c)$	[1]
C_P	= power input coefficient, $-< C_x \cdot \dot{h}^* >$	[1]
C_x	= lateral force coefficient, $F_x/(0.5\rho_f U^2_{ref} c)$	[1]
E	= Young's modulus	[Pa]
f	= motion frequency	[1/s]
f_1	= first natural frequency of the wing	[1/s]
f_f	= fluid force on the wing	[N/m]
F	= force deforming the wing	[N]
F_i	= fluid force acting on the wing	[N]
h	= plunge motion of the wing	[m]

* Postdoctoral Research Fellow, Department of Aerospace Engineering, University of Michigan, AIAA Member
† Provost & Chair Professor, Department of Mechanical Engineering, Hong Kong University of Science and Technology; also Adjunct Professor, Department of Aerospace Engineering, University of Michigan, AIAA Fellow

h_a	= plunge amplitude	[m]
h_s	= thickness of the wing	[m]
k	= reduced frequency, $\pi fc/U_{ref}$	[1]
p	= pressure	[Pa]
Re	= Reynolds number, $\rho_f U_{ref} c/\mu$	[1]
t	= time	[s]
St	= Strouhal number, fh_a/U_{ref}	[1]
T	= temporal part in method of separation	[1]
U_{ref}	= reference velocity: $2\pi fh_a$ for hover	[m/s]
u_i	= velocity vector	[m/s]
x_i	= position vector	[m]
w	= wing deflection	[m]
ϕ	= phase lag between plunge motion and pitch	[rad]
γ	= non-dimensional tip deformation parameter: $Stk(1+4\rho^* h_s^*)/\{\Pi_0(f_1^2/f^2-1)\}$	[1]
η	= propulsive efficiency: $\langle C_L\rangle/\langle C_P\rangle$	[1]
μ	= dynamic viscosity of fluid	[Pa s]
Π_0	= effective inertia, $\rho^* h_s^* (k/\pi)^2$	[1]
Π_1	= effective stiffness, $Eh_s^{*3}/(12\rho_f U^2_{ref} c^3)$	[1]
ρ_f	= density of fluid	[kg/m^3]
ρ_s	= density of structure	[kg/m^3]
ω_1	= non-dimensional first natural frequency: $2\pi f_1/f$	[1]
$(\cdot)^*$	= variables normalized either by c (length), $1/f$ (time), or ρ_f (density)	[1]
$\langle\cdot\rangle$	= time averaged variable: $1/f \int_0^{1/f} (\cdot)\, dt$	[1]

I. Introduction

Flapping motions are common to animal locomotion in air and water [1]. Birds or insects flap their wings interacting with the surrounding air to generate lift to stay aloft or produce thrust to fly forward [2]. Fish, on the other hand, swim by snaking or by fanning their fins in water [3]. Relation between the kinematics of wings or fins and the resulting aerodynamics has been considered extensively in the literature. A novel mechanism (clap and fling) [4] was found and unsteady aerodynamic mechanisms, such as the delayed stall due to leading-edge vortices (LEVs) [5], wake-capture and, rotational effects [6] were explained. The range of non-dimensional numbers relevant to the biological flappers was found as well: For the flapping motions with the frequency f and the amplitude h_a, the optimal Strouhal number, $St = fh_a/U_{ref}$, the ratio between the flapping wing velocity and the reference velocity U_{ref}, for cruise condition is $0.2 < 2St < 0.4$ [7]; the reduced frequency k is a measure of unsteadiness that compares the spatial wavelength of the flow disturbance to the chord c [8]. The operating reduced frequency, $k = \pi fc/U_{ref}$ of insects and birds [2] are $k < 0.25$ and those of fish [3] slightly higher at 0.5.

The aforementioned findings, however, are mostly based on a rigid wing framework, while the flapping wings and fins observed in the nature are flexible. For a variety of insects, the spanwise flexural rigidity of the wings is 1 or 2 orders of magnitudes greater than the chordwise flexural rigidity [9]. Fish fins are also highly flexible [10] and extreme deformations were observed during rapid movements [11]. The role that these flexibilities play on the aerodynamic performance has received great interest in the past decade [12,13,14,15]. The scaling laws that we developed previously [14] highlight multiple characteristics associated with the performance of a flexible, flapping wings in higher Reynold number regimes. For example, for a wing with the density ρ_s, Young's modulus E and thickness h_s, flapping in a fluid of density ρ_f, we used a scaling method to establish a relationship between the time-averaged force normalized by the effective stiffness, $\Pi_1 = Eh_s^{*3}/(12\rho_f U^2_{ref})$, which is the wing stiffness normalized by the fluid dynamic variables [12], and the non-dimensional tip deformation parameter, γ, defined as

$$\gamma = \frac{\left(1 + \frac{4}{\pi}\rho^* h_s^*\right)\cdot St \cdot k}{\Pi_0 (f_1^2/f^2 - 1)}, \tag{1}$$

where $\rho^* = \rho_s/\rho_f$ is the density ratio, $h_s^*=h_s/c$ is the thickness ratio, and $\Pi_0 = \rho^* h_s^* (k/\pi)^2$ is the effective inertia of the wing, and f_1 is the first natural frequency of the wing. Specifically, the scaling formula reads

$$\frac{\langle C_F \rangle}{\Pi_1} \sim \gamma \qquad (2)$$

where $\langle C_F \rangle$ is the force deforming the wing. For the hovering motions, $\langle C_F \rangle = \langle C_L \rangle \rho^*/h_a^*$, where ρ^*/h_a^* is the ratio between the inertial force and the aerodynamic force [14,16]. When a sinusoidal plunge motion is imposed at the leading-edge (LE) of the wing, the wing tip deformation of a linear elastic wing would then be proportional to γ. Based on this scaling relationship the propulsive force, power input, and efficiency and these three aerodynamic performance measures could be scaled. Consistent with those recently reported in the literature [13,14,16,17,18], the force scaling predicts that the maximum propulsive force, such as thrust in forward flight or lift in hover motion, is generated at a frequency which was only slightly lower than the natural frequency of the system. For the propulsive efficiency, numerical [19,20,14] and experimental [13,16] investigations using simplified geometries and kinematics revealed that the optimal frequency ratio, f/f_1, is in the range between 0.3 and 0.7. This correlates to the observations made for insects, e.g. dragonfly [13], moth [13], that the flapping frequency is below the natural frequencies of the wing, only a fraction of the resonance frequency. There are still several issues and uncertainties which need to be further investigated. For example, this scaling was derived from an assumption that $f/f_1 \ll 1$ and the data points were considered based on the configurations performed at $Re = \rho_f U_{ref} c/\mu$ on the order of 10^3 to 10^4, where μ is the viscosity of the fluid.

For hovering motions, the unsteady aerodynamics is influenced by multiple control parameters, including Reynolds number, flapping kinematics, environmental disturbances, such as the wind gust, and, of course, mechanical properties of the wing [21]. For example, the phase between translational and rotational motions of the flapping motion substantially affects the aerodynamic performance; turning the start of the wing rotation slightly before the stroke reversal could enhance the lift generation [6]. Unlike a rigid wing, for which both translational and rotational are controlled actively [6,21], a flexible wing can undergo passive pitch [22] due to combined aerodynamic loading and its inertia. The role of passive pitch on the performance of a flexible flapper has received great interest due to its perceived efficiency and relevancy to insect flight, which show large passive deformations while lacking in active control [23]. Also, in a much simplified but informative demonstration, at Re = 220 a flexible flapper, composed of two or three rigid components connected with a torsion spring, could save power compared to its rigid counterpart following the same kinematics, because passive deflection leading to passive pitch results in smaller drag and torque [23]. Similarly, at Re = 200, the lift generated by a hovering motion including passive pitch was sufficient to sustain lift for some insects [24]. Furthermore, at the Reynolds numbers between 20 and 120, a freely translating flexible plate, modeled by a rigid plate with a torsion spring acting about the pivot at the leading-edge (LE) of the plate, moved forward when $f/f_1 \ll 1$ and backwards otherwise [18,25], only by applying vertical heaving motions. The motion directions could also be related to the phase difference, ϕ, between the heaving and the passive pitch: forward if $\phi < \pi$ and backward when $\phi > \pi$. These studies highlight the interplay between the flexibility, the aerodynamic performance, and the structural response of a hovering flat plate at a low Re of $O(10^2)$, however the passive pitching is modeled with a torsion spring and the majority of the wing is assumed to be rigid, while real insect wings are not rigid and could reasonably be approximated with a homogeneous distribution of flexural stiffness [9].

In a recent study [14] we considered three flexible flapping wing configurations: i) plunging chordwise flexible airfoils in water in forward flight, ii) plunging spanwise flexible wings in water in forward flight, and iii) hovering isotropic Zimmerman wing in air, at $Re = O(10^3)$ to $O(10^4)$. On the other hand, we also highlighted the interplay between the kinematics and the resulting aerodynamic force and flow structures for a hovering rigid flat plate at Re = 100 [21]. In this study we extend our region of interest to the hovering kinematics of flexible flat plates at a lower Reynolds numbers of 100 to 1000. This study is aimed at bridging the gap between these two studies and broadening the applicability of the scaling laws developed. We consider a flexible flat plate undergoing a pure plunging motion at the LE of the flat plate and the interplay between the aerodynamic, inertia, and elastic restoring forces will lead to passive pitch. The current setup is inspired in part by an experiment on a free-to-move plunging rigid wing in water [26] that showed intriguing fluid dynamics features: When the flapping frequencies are below a threshold value, i.e. Re < 390, the wing remained stationary in the horizontal plane and the wakes shed in the flow form a symmetric structure. For the frequencies above this threshold value, such that Re > 390, the symmetry of the wake breaks, resulting in an inverted von Kármán vortex street, that is indicative of propulsion: the flapper moves forward. We focus on the time-averaged lift, <C_L>, which is required to compensate the weight of a hovering animal and the propulsive efficiency, η, which is defined as the ratio between <C_L> and <C_P>, the time-averaged power input, as a function of Π_1 and k. Note that for insects [27], with a notable exception of butterfly [27], whose wing masses are typically of only few percent of the entire body mass, the flapping time scales are much shorter than that of the entire body. From a vehicle dynamics viewpoint, the time-averaged flapping wing aerodynamic parameters are of substantial interests. Hence, even though unsteady mechanisms are highly responsible for the aerodynamic outcome of a low Reynolds number flapping wing, the time-averaged values can be used to guide the search for favorable flapping and materials parameters. The results are discussed by expanding the scaling with the non-dimensional tip deformation parameter previously proposed [14] while focusing on the effects of the flexibility on the phase dynamics between the plunge and the passive pitch. While experimental investigations [28,29,30] of effects of flexibility is an active field of research, here, we employ a carefully validated fully-coupled Navier-Stokes equation solver and a linear beam solver [14]. By varying the Young's modulus of the flat plate and the plunging amplitude, the design space (Π_1, k) is populated with training points. We use the surrogate models techniques [21] for the objective functions <C_L>, <C_P>, and η to effectively organize the data and discuss the qualitative trend.

II. Methodology

A. Non-dimensional Governing Equations and Kinematics

The resulting governing equations for the incompressible fluid modeled by the unsteady two-dimensional Navier-Stokes equations with constant fluid density ρ_f and viscosity μ are

$$\frac{\partial}{\partial x_i^*}(u_i^*) = 0 \tag{3}$$

$$\frac{k}{\pi}\frac{\partial}{\partial t^*}(u_i^*) + \frac{\partial}{\partial x_i^*}\left(u_j^*\, u_i^*\right) = -\frac{\partial p^*}{\partial x_i^*} + \frac{1}{Re}\frac{\partial}{\partial x_j^*}\left\{\frac{\partial u_i^*}{\partial x_j^*}\right\} \tag{4}$$

where $(\cdot)^*$ indicates the non-dimensional variables. The variables are non-dimensionalized with the reference velocity, U_{ref}, as the velocity scale, inverse of the motion frequency, $1/f$ as the time scale, and the chord, c, as the length scale. For forward flight the forward velocity of the wing, i.e. the incoming velocity in the frame of reference of the wing, would have been chosen as U_{ref}, however in hover such a freestream is absent and the maximum translational velocity of LE is taken as the reference velocity.

A horizontal sinusoidal prescribed motion is imposed on the leading edge (LE) of the flat plate as

$$h^*(t^*) = St\frac{\pi}{k}\cos(2\pi t^*), \tag{5}$$

see also Fig. 1. The Strouhal number St appears in combination with k giving the non-dimensional plunge amplitude $h_a^* = h_a/c = \pi\, St/k$. The Reynolds number Re is the ratio between the inertial and the viscous forces in the fluids. Since $U_{\text{ref}} = 2\pi f h_a$ is the maximum translational velocity, we have $k = \pi f c/(2\pi f h_a) = 1/(2h_a^*)$, $Re = \rho_f(2\pi f h_a)c/\mu$, and $St = f h_a/(2\pi f h_a) = 1/(2\pi)$. Because of the absence of the freestream, the Strouhal number loses its meaning for hover.

We consider a flat plate of uniform thickness oriented vertically. As the flat plate follows the imposed horizontal motion, Eq. (**5**), at the LE, the resulting fluid dynamic force dynamically balances with the wing inertia and the elastic bending forces, modeled locally as a linear Euler-Bernoulli beam,

$$\Pi_0\frac{\partial^2 w^*}{\partial t^{*2}} + \Pi_1\frac{\partial^4 w^*}{\partial x_2^{*4}} = f_f^*, \tag{6}$$

where w is the wing deflection due to bending motion and f_f^* the distributed transverse fluid force on the wing per unit span. The aerodynamic force is normalized with $\rho_f U_{\text{ref}}^2 c/2$, e.g. $C_L = -2F_2/(\rho_f U_{\text{ref}}^2 c)$ where $-F_2$ is the lift force. The aerodynamic force on the flat plate is decomposed in the lift direction, C_L, and the lateral direction, C_x, see also Fig. 1.

Finally, the time-averaging operator < · > is defined as

$$\langle C_L \rangle = f \int_{m/f}^{(m+1)/f} C_L \, dt, \tag{7}$$

for example, for C_L. The resulting force was not periodic in time and to have a representative value for the time averaged force and to avoid initial transient effects, we chose for $m = 3$. In the subsequent presentation of results the non-dimensional time, $t^* = 0.0$ represents the start of the third cycle, unless otherwise stated. For a more comprehensive treatment of the dimensional analysis and non-dimensionalization we refer to our previous work [14].

B. Numerical Models

The governing equations for the fluids given by Eq. (3) are solved with Loci-STREAM [31,32,33], which is a three-dimensional, unstructured, pressure-based finite volume solver written in a rule-based framework. It employs implicit first or second order time stepping and treats the convection terms using the second order upwind-type scheme and the pressure and viscous terms using second order schemes. The system of equations resulting from the linearized momentum equations are handled with the symmetric Gauss-Seidel solver. The pressure correction equation is solved with either the GMRES linear solver with the Jacobi preconditioner provided by PETSc [34,35,36], or the BoomerAMG [37] linear solver provided by hypre. The LOCI-framework is by design rule-based highly parallelizable framework for finite volume methods [38]. The geometric conservation law [39], a necessary consideration in domains with moving boundaries, is satisfied [40]. The mesh deformations are realized using radial basis function (RBF) interpolations [41].

An Euler-Bernoulli beam model has been incorporated to solve Eq. (6) using a finite element representation. The structural damping is not considered in this study. Two degree of freedom, i.e. displacement and bending, are allowed at each node. The Newmark time integration scheme is employed. Computations done for a flexible airfoil composed of a rigid teardrop and elastic flat plate at higher Reynolds number and for various motion frequencies [14] showed that a linear Euler-Bernoulli beam is sufficient for qualitative analysis of the fluid-structure interaction coupling.

The fluid-structure interaction is based on a time-domain partitioned solution process in which the partial differential equations governing the fluid and the structure are solved independently and spatially coupled through the interface between the fluid and the structure. An interface module is added to the fluid solver to communicate the parallelized flow solutions on the three-dimensional wetted surface to and from the serial structural solver. At each time step the fluid and the structural solvers are called one after the other until sufficient convergence on the displacements on the shared boundary surface are reached in an inner-iteration before advancing to the next time step. Full details of this algorithm and careful validation analysis against well-documented experimental results can be found in our previous work [14].

C. Case Setup

We consider a flow with unit density initiated by a hovering two-dimensional flat plate with unit chord with the thickness ratio of $h_s^* = 0.02$ with flat edges. The fluid flow is computed by solving Eq. (3) with the finite volume method described in Section II.B. The direction of the motion and the computational mesh is shown in Fig. 1. We focus mainly on the Reynolds number regime of a fruit fly: $Re = 100$, but also consider $Re = 1000$ to assess the sensitivity of the aeroelastic response to the change in the Reynolds number.

The flat plate is modeled with 51 nodes equally distributed over the flat plate. The maximum translation velocity of the flat plate is such that the reference velocity $U_{\mathrm{ref}} = 2\pi f h_a = 1$. The density ratio is 7.8, similar to steel in water or a light material in air. The case of $\rho^* = O(10^3)$, which is more characteristic of an insect wing in air was studied previously [14] and the density ratio effect is discussed briefly in Section III.G.

The remaining non-dimensional parameters, i.e. the effective stiffness Π_1 and the reduced frequency k, are varied by changing the Young's modulus E and the plunge amplitude h_a, respectively, to probe their influence on the resulting aerodynamics and the structural deformations. The range selection of h_a motivates from the plunge amplitudes observed from biological flyers [21]. It is reported in the literature that the natural flyers operate at $f/f_1 < 0.8$ [13] and in this study, we adjust the Young's modulus to follow a similar range: $0.04 < f/f_1 < 0.8$. These design variables and the remaining non-dimensional parameters considered are summarized in Table 1.

Surrogate models [21,42,43] are used to effectively organize the design space and to visualize the relationships between the design variables and the performance metrics. The objective functions are the time-averaged lift, $<C_L>$, the time-averaged power input, $<C_P> = <C_x \cdot \dot{h}^*>$, and the propulsive efficiency, $\eta = <C_L>/<C_P>$. The initial design of experiments used a Face Centered Cubic Design [43] and the Latin Hypercube Sample algorithm [42] was employed to fill the remainder appropriately. The resulting design space is extended and refined to capture the area of higher lift, power input, and efficiency. In total 27 training points are selected. The design space along with the frequency ratio, f/f_1, is depicted in Fig. 2. See Appendix B for the detailed setup of the employed surrogate models and the error metrics.

III. Results and Discussion

A. Aerodynamic Performance of a Hovering Flexible Flat Plate

The resulting surrogate models for $<C_L>$, $<C_P>$, and η as a function of Π_1 and k are shown in Fig. 3 for $Re = 100$ and 1000. All other parameters are kept constant. At $Re = 1000$ $<C_L>$ and η have slightly higher values than at $Re = 100$, while $<C_P>$ is similar. The overall qualitative trends remain similar. Hence, for now we focus on $Re = 100$ cases and we discuss the Reynolds number effect in Section III.D in more detail.

The range of design space is explained in Section II.C and the process of surrogate construction is described in Appendix B. In the right bottom corner of the design space the lift generation is low corresponding to an almost rigid flat plate. As f/f_1 increases, see also Fig. 2, $<C_L>$ increases. When $0.3 < f/f_1 < 0.4$, the lift is the highest. As f/f_1 increases further and approaches 1, lift decreases again. The observation that the maximum lift is generated when $0.3 < f/f_1 < 0.4$ is rather surprising and contradicts our previous scaling prediction that the maximum propulsive force is predicted near $f/f_1 = 1$ [14] and that the best performance is obtained at the resonance [20]. This discrepancy will be explained in Section III.F. Figure 2 also illustrates that the qualitative trend of lift seems to depend on f/f_1 but the frequency ratio is not the main parameter: the maximum force is generated when both Π_1 and k are high in the considered design space. In particular among the training points the highest lift computed was $<C_L> = 1.78$ for $\Pi_1 = 1.7$ and $k = 2.0$ in the top right corner.

To illustrate the interplay between the kinematics, wing deformation and the resulting force, we have plotted the vorticity field, flat plate shapes, and force histories for the maximum lift case ($\Pi_1 = 1.7$, $k = 2.0$) in Fig. 4. Vorticity accumulates at the LE, which is indicative of formation of a LEV near the stroke ends ($t^* = 0.0, 0.5$), however it does not detach from the flat plate. Rather a strong trailing-edge vortex (TEV) of the opposite direction interacts with the previously shed wakes resulting in a vortex structure that is favorable for downward momentum jet. The time-dependent lift coefficient is positive, hence this case is lift producing throughout the whole stroke except at the stroke ends and consists of two peaks, both reaching its maxima at the mid-strokes ($t^* = 0.25, 0.75$). The first lift peak at $t^* = 0.25$ is 4.7, and the time-averaged value is 1.78. Lift of such magnitude would support the weight of a tethered hovering *Drosophila* spp., which would require $<C_L>$ of 1.6 [44]. At the stroke ends, the flat plate is almost vertical while during the mid-strokes the pitch angles are higher. The resulting motion is that of a normal hovering that is observed for many hovering flyers [4] with synchronized (symmetric) rotation. A striking feature of this case is that unlike the normal hovering motions studied with a dynamically scaled robofly [6] at $Re = O(10^2)$, the lift history for the current study is without any distinct wake-capture peak. The absence of the wake-capture peak can be explained from the vorticity fields that the LEV does not detach and the TEV is convected downstream, hence the wing-wake interaction does not take place. Another difference compared to the lift generated by the robofly is that the lift peak at the stroke ends corresponding to the synchronized rotation [6] is not observed for this case. A plausible reason is that the wing rotation was controlled actively in the case of the robofly, while any resulting pitching motion is passive here. The phase lag between the translation and the passive pitch is discussed more in Section III.E.

The resulting power input (Fig. 3b) depicts similar trend as $<C_L>$. Compared to other regions, for the cases located in the upper right region where the highest lift is generated, we see that the required power input is also the highest. This is reflected in the surrogate response for η that the region of high lift does not correspond to high efficiency. Similar to lift, $<C_P>$ is the highest when $0.3 < f/f_1 < 0.5$, but as we move toward low k and low Π_1, $<C_P>$ drops faster than $<C_L>$. Thus it is not surprising that the ratio between lift and power required, η, is the highest around $\Pi_1 = 0.3$ and $k = 0.7$. To highlight the fluid-structure interaction in this high efficiency region, the flow field and the aeroelastic responses are illustrated in Fig. 5 for the case with the highest $\eta = 0.66$ ($\Pi_1 = 0.3$, $k = 0.6$). The resulting flat plate motion is also a synchronized rotation hovering similar to the maximum lift case. The instantaneous lift for this case is always positive and it is still without a wake-capture peak. The maximum and time-averaged lift values are smaller: 3.4 and 1.45, respectively, compared to the maximum lift case. However, the lateral force, C_x, which is representative for the power input is also much smaller, yielding higher efficiency. Because $k = c/(2h_a)$ is lower than the maximum lift case, h_a is larger, resulting in wake structures with vortices further apart. These vortices form a row of alternating vortices favorable for propulsion, resembling the inverted von Kármán vortex street, which are characteristic for optimal propulsion [45,18].

B. Effects of Effectiveness Stiffness, Π_1, and Reduced Frequency, k

To assess the effects of each parameter, k and Π_1, on the resulting aerodynamics with respect to the maximum lift case (k=2.0, Π_1 = 1.7) at Re = 100, we consider the variation in the vorticity field and the forces for the cases k = 0.6, 1.3, and 2.0 at constant Π_1 = 1.7 and Π_1 = 1.7, 1.0, and 0.3 at constant k = 2.0. The former fixes the wing stiffness and vary the plunge amplitude to consider the effects of kinematics, while for the latter we assess the parametric influences of the stiffness at constant normalized plunge amplitude of 0.25.

Figures 6a-c) shows the vorticity field around the flat plate with varying k while holding Π_1 constant. Seven vorticity field contours during the backstroke illustrate the time evolution of the vortical structure. Recall that the reduced frequency is a measure for the unsteadiness and in hovering it is inversely proportional to the normalized plunge amplitude. At k = 2.0, the corresponding plunge amplitude is 0.25 and the LEV has barely time to develop and to detach from the flat plate, while a well-defined TEV forms at the TE where the amplitude is larger due to deformation and sheds into the wake, as discussed earlier. As k decreases to 1.3, the size of the LEV increases. The deflection of the TE is smaller at the mid-stroke, but larger at the end of the stroke. The phasing between the TE and the LE resembles that of an advanced rotation mode. At k = 0.6 as the flat plate reverses its direction, the LEV formed in the previous stroke interacts with the LEV which is in development. Meanwhile, a larger TEV forms at the TE of the flat plate, which also interacts with the LEV. The LEV and the TEV form a vortex pair. This vortex pair convects in diagonal direction, which results in a vortex formation that is not favorable for lift generation. This is confirmed in the instantaneous lift history depicted in Fig. 7a). Whereas both k = 2.0 and 1.3 show one peak per stroke, at k = 0.6 the magnitude of the lift is smaller and more complex due to the vortex-vortex and vortex-wing interaction. Interestingly, for this advanced rotation mode shown at k = 1.3, the resulting lift is also in phase advance compared to the synchronized rotation mode at k = 2.0.

When Π_1 is reduced with respect to the maximum lift case (Π_1 = 1.7, k = 2.0), the resulting vortical structures remain qualitatively similar. Reducing Π_1 yields in a normal hovering motion with delayed rotation in which the reversal of the stroke at the TE occurs later than the LE: at Π_1 = 0.3, the flat plate is almost vertical at the mid-stroke. Furthermore, the size of the vortices reduces with decreasing Π_1. These observations are also illustrated in the resulting time history of lift in Fig. 7b). Reflecting the smaller size of the vortices, the lift reduces with decreasing Π_1 and the delayed rotation mode results in the phase lag in lift compared to the synchronized rotation mode.

C. Symmetry-breaking by Flexibility enhances Performance

When a rigid wing, that is designed to move freely in horizontal direction in still water, plunges vertically at low motion frequencies the resulting vortical structures are symmetric, hence keeping the wing stationary at its position [26]. However above certain frequency, the wing starts to move forward while breaking the symmetry of the vortex formation. This bifurcation phenomenon can be characterized with the Reynolds number defined as $Re_f = \rho_f f h_a c/\mu$, which is proportional to the one employed in this study by a factor of 2π. When the rigid wing is replaced with a flexible plate with the same geometry but with lower E, the resulting forward speed was significantly greater than that of the rigid wing [46].

The time history of forces for a rigid hovering flat plate at k = 0.25 and k = 2.0 at Re = 100 is depicted in Fig. 8a,b). At k = 2.0 the lift remains zero, whereas the lateral force oscillates up and down. The corresponding vorticity field (Fig. 8c) shows that the vortex shedding behavior is symmetric with respect to the flat plate: the LEV and TEV form and interact with the vortices in development. Subsequently, the vorticity shed by the flat plate form a symmetric structure with pairs of alternating vortices. When k = 0.25, the lift again remains small but only until the third motion cycle. Then the symmetry breaks and the vortices start to convect in diagonal directions (Fig. 8d). Any disturbance in the flow field results in the breakdown of the symmetric vortex formation and the unsteady lift starts to oscillate. The LEV and the TEV are now aligned with an angle of approximately 45 degrees with the hovering motion and the resulting lateral force is smaller than at k = 2.0. This symmetry breaking behavior is similar to the phenomenon described observed in a water tank for a rigid wing [26]. It is interesting to note that in our study the bifurcation behavior seems to be described by the reduced frequency k and only the Reynolds number, which is fixed at 100 here.

For a flexible flat plate, the unsteady lift increases with an order of at the same k and Re, e.g. Π_1 = 1.7 and k = 2.0 (Fig. 4). The deflection of the TE introduces a symmetry-breaking disturbance into the flow and positive unsteady lift is created immediately after t^*. Moreover, the magnitude of the lateral force is similar to its rigid counterpart, suggesting better propulsive efficiency for a flexible flat plate over its rigid counterpart.

D. Reynolds Number Effects

The effects of the Reynolds number on the aerodynamics of flapping flyers have attracted numerous investigations [2]. In particular, the stability and the existence of spanwise flow in the LEV, which is considered as one of the main unsteady mechanisms for lift enhancement, have received substantial attention [47,48]: In particular as Re changes, the flow topology and forces respond differently. At the Reynolds number relevant to a hovering hawkmoth, Re = 4000 to 6000, an intense and conical LEV was observed on the wing with significant spanwise flow [48]. At a lower Reynolds number e.g. corresponding to a hovering fruit fly, Re = 120, on the other hand, such spanwise flow was weaker and the vortex structure was simpler [47,48]. However, many of these studies assume rigid wing structures and neglect the wing flexibilities.

We employ two-dimensional computations at two Reynolds numbers of 100 and 1000 for a flexible flat plate. An earlier study [47] showed that the net force coefficients were slightly higher at Re = 1400 than at Re = 120 corresponding to comparatively greater vorticity production with more complex structure in the flow. Similarly, Fig. 3 indicates that the resulting lift is slightly higher at Re = 1000 than at Re = 100. At Re = 1000 time-averaged lift coefficient as high as 2.36 was observed (Π_1 = 1.7, k = 1.65). For example, for the case with the highest lift of 1.78 and η = 0.34 at Re = 100 (k = 2.0, Π_1 = 1.7), $\langle C_L \rangle$ and η increase to 2.28 and 0.44, respectively, at Re = 1000.

Figure 9 shows the vorticity field, force time history, and flat plate shapes for the case with the highest η at Re = 100 (case 29: Π_1 = 0.3, k = 0.6) for both Reynolds numbers. The vorticity produced in the flow at Re = 1000 is stronger and confined in a smaller region. The global flow structure remain similar, but at Re = 1000 the flow pattern consists of smaller but more vortex structures. Furthermore, as illustrated in Fig. 9c), the deformation of the flat plate remains similar, hence the resulting lift coefficients are also close, i.e. 1.45 and 1.47, respectively. Comparing the instantaneous force histories demonstrates that the lateral force is similar both in magnitude and shape, although at Re = 1000 there is a slight phase lag. For the lift, the time-averaged value is close, but at Re = 100 the lift response is asymmetric, while at Re = 1000 symmetric: some cases showed symmetric, others asymmetric lift response at this motion cycle. Whether the force response of a flexible flapping wing should be periodic or symmetric or not is an interesting yet open question and will be left as a future study.

E. Passive Pitch and Phase Control

Most insects including flies, bees, and wasps, employ a normal hovering, in which they flap their wings in a horizontal plane [4,49]. Usually both forward and backward strokes are symmetric, generating lift in both strokes. Other hovering modes exist, e.g. the inclined hovering used by the hoverflies [49,50,51] and dragonflies [49] in which the most of the lift is generated during the downstroke, or the water-treading mode [52] in which the delayed stall mechanism plays the main role. For normal hovering, stroke plane deviation including the figure-8 motions are also reported [44,53] for biological flyers. Here, we focus on normal hovering and the relation to passive pitch.

When both translation and rotation were actively imposed on a rigid dynamically scaled *Drosophila melanogaster* robofly in normal hovering mode at Re = O(10^2), the resulting motion and aerodynamic force could be categorized into three modes [6]: the advanced rotation mode in which the wing starts to rotate before the wing reverses its translational direction, the synchronized (symmetric) mode where the wing alignment is vertical at the end of strokes, and the delayed rotation in which the wing rotates after the stroke reversals. Force measurements [6] found out that the advanced rotation increased the rotational force at the ends of each stroke while the rotational force was slightly smaller for the synchronized and even negative for the delayed modes.

All three modes were observed due to passive pitch for the hovering flat plate. To provide a more systematic picture of how the phase relationship depends on the wing flexibility, we determined for each Re = 100 case the phase relationships and mapped these modes onto the design space in Fig. 10a). In the bottom right region with high Π_1 and low k, where the flat plate is almost rigid the normal hovering modes are found as the stiff wing hardly deflects. As k increases and Π_1 reduces the deformations of the flat plate increases leading to the advanced rotation mode. Moving in the same direction, the phase advance of the passive pitch to the translation decreased, resulting first in the synchronized hovering mode and then finally in the delayed rotation mode. Figures 10c-e) illustrate the flat plate shapes of the representative cases for each mode. Because the qualitative distribution of these phase modes resembles the frequency ratio distribution in the design space, see Fig. 2, we plotted the phase angle, ϕ, for each case against f/f_1. The phase angle is determined by computing the angle between the TE and the LE at the stroke ends. Indeed, as f/f_1 increases ϕ increases at first resulting in the advanced rotation mode, and then ϕ starts to decrease yielding the synchronized mode and the delayed rotation modes.

Similar observations were reported previously [18,24,23]: For a freely moving flat plate with a torsional spring at its LE, the vertical plunging motion resulted in a forward motion with advance phase shift when $f/f_1 < 1$ and a backward motion with delayed phase shift for $f/f_1 > 1$. Similar phase shift was proposed using a simplified lumped-torsional-flexibility model and for a rigid flat plate with a flexible LE to introduce passive pitch, a normal hovering motion at $f/f_1 = 0.31$ at $Re = 290$ resulted in an advanced rotation mode [24]. The difference in the observed phase shift frequency ratio may be ascribed to the difference in the structural modeling: torsional spring at the LE of a rigid flat plate compared to continuous elastic flat plate that we employed here.

For a two component rigid elliptic wings linked with a torsional spring, when the phase difference between the translation and pitch was synchronized, the highest efficiencies were obtained, up to 0.8 at $Re = 220$ and $\rho^* = 5$ [23]. Recall that in an extensive experimental study with hovering rigid wings at $Re = O(10^2)$ for synchronized rotation modes pitching angle of 45 degrees produced the highest lift, whereas for the advanced rotation mode the lift was similar at 1.9 [44]. For an elastic flat plate, both the maximum lift (Fig. 4) and the optimal efficiency (Fig. 5) cases also show synchronized hovering modes. The maximum translational velocity is found at the midstroke, where the angle the flat plate makes with its translating motion is around 45 degrees, see Figs. 4b) and 5b). In absence of both wake-capture and rotational force effects, synchronizing the highest pitching angle at the maximum translational velocity is beneficial. This result also agrees with the observations [25] made for a plunging rigid airfoil with torsion spring at its LE that the case with the best performance is seen with a phase lag of approximately 90 degrees and the maximum angle of attack at the maximum plunging velocities. As the maximum pitching angle is at the midstroke and assuming a nearly periodic motion for the TE displacement, the TE and LE should then in phase at the ends of the stroke. This is confirmed in Fig. 10f) where the time histories of TE displacement relative to the LE displacement, w_{rel}, are plotted for the three rotation modes. For the synchronized rotation case, w_{rel} is near zero at the stroke ends and close to 1 at the mid-stroke. As w_{rel} is normalized by the chord, the pitching angle at $w_{rel} = 1$ is 45 deg. For the advanced rotation case, the relative deformation of the TE is smaller, resulting in smaller pitching angles during the strokes and this case yields in smaller lift coefficient. Finally, although the delayed rotation case has a larger w_{rel} than the advanced rotation case, the time instant of the maximum relative deformation lags far behind: the relative deformation at the midstroke is for example close to zero, which means that the flat plate is almost vertical during the midstroke. The lift coefficient for the delayed rotation case is the lowest among the three considered.

These results suggest that at these Reynolds numbers when the only rotational mechanism is due to passive pitch, then the optimal aerodynamic performance correlates to synchronized rotation motion and the phasing can be controlled by adjusting the frequency ratio. This idea can be readily adapted for developing flapping wing MAVs. One of the main challenges of designing flapping MAVs is the weight penalty from implementing the two motion actuators, one for translation (or flapping) and one for pitching. By selecting the appropriate material and adjusting the flapping motion frequency to match the desired frequency ratio, this study suggests lift coefficients up to 1.78 could be obtained at $Re = 100$ and 2.36 at $Re = 1000$ or high propulsive efficiencies from 0.66 to 0.90.

F. Revised Scaling for Aerodynamic Performance

We previously analyzed various flexible flapping wing configurations and proposed a scaling parameter, γ, which denotes the non-dimensional tip deformation, as expressed in Eq. (1), where $(2\pi f_1/f)^2 = k_1^4\Pi_1/\Pi_0$ with k_1 being the eigenvalue corresponding to the first spatial beam mode [14]. Note that in hover St is a constant. In this study ρ^* and h_s^* are fixed, hence γ is only a combination of k, and Π_1. Furthermore, by considering the non-dimensional energy balance on the deforming wing we established a scaling relationship Eq. (2) for the propulsive force [14].

One of the approximations made in the previous derivation was that $f/f_1 << 1$. We applied the scaling relationship given by Eq. (2) to the cases considered in this study. For the cases with $f/f_1 < 0.6$, Eq. (2) indeed resulted in a linear trend in the log-log axis, confirming the scaling. However, for the cases with $f/f_1 > 0.6$ (cases: 2, 21, 26, and 27), γ was higher but now $<C_F>/\Pi_1$ decreased. To account for the higher frequency ratios, but still in the domain of $f/f_1 < 1$, we propose a revised scaling relationship as follows. We argued previously that the temporal part of the wing tip, T, would scale as

$$T(t^*) \sim \gamma\{\cos(2\pi t^*) - \cos(\omega_1 t^*)\}, \tag{8}$$

where $\omega_1 = 2\pi f_1/f$ is the first non-dimensional natural frequency. Instead of approximating the wing tip velocity scale as $\omega_1\gamma$, which is only valid for $f/f_1 << 1$, we let it to scale as $2\pi\gamma$, which could also be interpreted as the wing tip velocity scaling being proportional to the ratio between the tip deflection, γ, and the non-dimensional motion period. Then, the non-dimensional energy balance leads, without making further approximations, to

$$\frac{\langle C_F \rangle}{k_1^4 \Pi_1 - 4\pi^2 \Pi_0} = \frac{\langle C_F \rangle}{\Pi_1\{1-(f/f_1)^2\}} = \frac{\langle C_L \rangle}{\Pi_1\{1-(f/f_1)^2\}} \frac{\rho^*}{h_a^*} \sim \gamma. \tag{9}$$

Compared to Eq. (2), Eq. (9) has a corrector for the frequency ratio effects. Note also that when $f/f_1 \to 0$, Eqs. (2) approaches to Eq. (9). When f/f_1 small the term with Π_1 dominates over the term with Π_0, implying the work done on the wing is mostly in balance with the restoring elastic force. As f/f_1 increases the Π_0 term cannot be neglected anymore. Figure 11a) shows the scaling relationship given by Eq. (9). The trend of $\langle C_L \rangle/\beta_1$ is monotonic with γ in log-log scale, where $\beta_1 = \Pi_1\{1-(f/f_1)^2\}h_a^*/\rho^*$. Closer examination of the trend shows that around $\gamma = 1$ the slope of the trend changes. For each slope a linear fit calculated as:

$$\frac{\langle C_L \rangle}{\beta_1} = \begin{cases} 10^{1.4}\,\gamma^{2.0} & \text{for} \quad \gamma < 1 \\ 10^{1.8}\,\gamma^{0.34} & \text{for} \quad \gamma > 2 \end{cases} \tag{10}$$

excluding the cases in transition for *Re* = 100. The resulting coefficients of determination were 0.98 and 0.83, respectively. The addition of the frequency ratio corrector and the decrease of the slope have an interesting consequence for the frequency ratio at which the maximum propulsive force is generated. Keeping all other parameters fixed and by only considering the frequency ratio effects, we see that when $\gamma < 1$, hence at small frequency ratios, the maximum force is generated at $f/f_1 = 1$. However, strictly speaking as $f/f_1 = 1$ violates the assumption of the small frequency ratios, we need to take the smaller slope, yielding the maximum force frequency ratio of 0.6: when $f/f_1 > 0.6$ the performance starts to drops. The value $f/f_1 = 0.6$ slightly overpredicts the frequency ratios at which the largest lift are seen in Fig. 3. Although this scaling relation is promising and captures the main trend, it does not capture all the details involving nonlinear physics including damping. Still, for a self-propelled insect model [13] the best performance was observed at $f/f_1 = 0.7$ and the performance decreased by a factor of more than 4 at $f/f_1 = 1$. In our configuration the wing is in hover mode, rather than in forward flight, the current discussion also suggests that the maximum lift may be obtained at a frequency ratio well below the resonance condition. The scaling for the power input remains the same and the propulsive efficiency changes following the revision for $\langle C_L \rangle$ [14], see Fig. 11b,c), with $\beta_2 = \Pi_1^2/\{k^2(1+4\rho^* h_a^*/\pi)\}$ and $\beta_2 = Stk\,(1+4\rho^* h_a^*/\pi)/[\Pi_1\{1-(f/f_1)^2\}\gamma^2\}]$. Plotting the current propulsive force scaling with the previous data set [14] including the plunging chordwise flexible airfoils and spanwise flexible wings in water in forward motion, the hovering isotropic wings in air, and some insects fall altogether on an almost linear line, see Fig. 12.

G. Swimming vs. Flying

Another interesting outcome of the scaling is found in the definition of γ given by Eq. (1). For an insect wing flapping in air $4\rho^* h_a^*/\pi$ is of the order $O(10^2)$ to $O(10^3)$. This means that $4\rho^* h_a^*/\pi$, which is from the inertia force, is much greater than 1, which is the term from the fluid dynamic force approximated by the added mass [14]. This is consistent with the previous findings that for high density ratio systems the majority of the wing bending is due to inertial forces [54]. For an isotropic Zimmerman wing hovering in air the inertial force was more dominant and the scaling given by Eq. (9) applied well. On the other hand, when ρ^* is low, such as for fish in water, the fluid dynamic forces become more dominant. In this study $4\rho^* h_a^*/\pi = 0.12$, comparable to a steel wing in water, the added mass force is largely responsible for the wing bending. Figure 12 includes hovering motions in both air and water, suggesting $\rho^* h_a^*$ indeed acts as the main parameter that characterize whether the added mass is more important or the inertial force.

It should be, however, noted that a fish does not need to generate lift. Unlike flyers that must create a lifting force to sustain its weight to stay aloft, fish float using buoyancy: The fanning of fins is mainly to produce locomotion. Hence, the normal hovering motion including passive pitch studied here may only be applicable for a fictitious swimmer; still current analysis highlights the difference and similarities in swimming and flying as illustrated in Table 2. Although both types of forces are acceleration dependent, the condition for optimal performance is different. Present discussion suggests that this difference in optimal conditions is related to how a wing or a fin is deformed and its consequence on the aerodynamic performance and detailed analyses of this intriguing aspect of swimming vs. flying will be reported in the future.

IV. Summary and Concluding Remarks

This study addresses the effects of flexibility on a hovering flat plate at Re = 100 and 1000. A horizontal sinusoidal plunging motion is imposed at the LE of the flat plate, which leads to passive pitching. By employing a fully coupled Navier-Stokes equation solver and Euler-Bernoulli beam solver, the lift, power input, and propulsive efficiency are investigated. We observe the following points.

1. The scaling relationship between the non-dimensional tip deformation and the time-averaged force responsible for wing deformation normalized by effective stiffness still holds. While the previous relationship was limited to $f/f_1 << 1$, by scaling the tip velocity with the ratio between the tip deflection and the unit period results in a revised scaling relationship that covers wider range of frequency ratios.
2. For both Reynolds numbers, the surrogate model response show that the high lift region in the design space correlates with high power required. The highest lift is obtained when the wing flaps with high frequency with short plunge amplitude (high k) with stiffer wing (high Π_1), while a slower motion over larger plunge amplitude (lower k) with softer wing (lower Π_1) yields the highest efficiency. For both cases the motion frequency is only a fraction of the first natural frequency around 0.3 to 0.4, disagreeing with the popular belief that the resonance condition correlates with better performance. For higher frequency ratios the motion yields in a delayed rotation mode which results in worse performance. The revised scaling relationship overpredicts the maximum force generation at f/f_1 = 0.6.
3. The overall aerodynamic performance as well as the resulting flow structures remains essentially the same for the Reynolds number range considered. Increasing Re to 1000 from 100 yields slightly higher lift, 1.78 to 2.36, respectively, while maintaining similar power required. The resulting efficiency hence is higher at Re = 1000: 0.66 vs 0.90. The overall vorticity structures are similar, but at Re = 1000 the vortices are more concentrated in a smaller vortical structures.
4. Normal hovering motions at Re on the order of 100 for rigid wings exhibit unsteady lift enhancement mechanisms, such as rotational lift and wake capture at the stroke ends. However, for flexible hovering flat plates where the rotational motion is solely due to passive pitch, both unsteady force mechanisms are absent. Furthermore, the highest lift and the optimal efficiency motions resemble that of synchronized rotation with flat plate almost vertical at the stroke ends. A plausible reason for such synchronized rotation mode is to yield maximum pitching angle of 45 degrees at the midstroke, which is known to be a high lift producing kinematics for rigid wings.
5. A consequence of the applicability of the proposed scaling relationship is that when the density ratio is low, such as in water the wing shape is determined by the acceleration-reaction force, while in air the wing is deformed via its inertial force. The condition for optimal performance is different for swimming and flying because different types of force are responsible for wing deformation. Detailed interaction between the flexibility, density ratio, and the aerodynamic performance will be assessed in the future.

In summary, the interplay between the wing motion, wing flexibiltiy, and resulting aeroydnamics is evinced for flexible flat plate in hover. In contrast to previous studies in which the passive pitch is modeled with a torsion spring at the leading edge of a rigid flat plate, here we assume an elastic flat plate. By adjusting the plunge amplitude, the motion frequency, and the wing flexibility either high lift or high efficiency motion can be achieved without use of active rotational mechanism. For both motions the frequency ratio was around 0.3 to 0.4 and the phase between plunge and passive pitch a synchronized rotation mode. A revised scaling relationship is established for the non-dimesional wing tip deformation parameter, which is a combination of *a priori* known wing geometry, structural properties, and motion amplitude and frequency. Current results help to gain more understanding in the role of passive pitch in hovering conditions and provide insights that can guide the design of flapping wing micro air vehicles.

Acknowledgments

This work has been supported in part by the Air Force Office of Scientific Research's Multidisciplinary University Research Initiative (MURI) grant and by the Michigan/AFRL (Air Force Research Laboratory)/Boeing Collaborative Center in Aeronautical Sciences. We thank Hikaru Aono for his fruitful suggestions.

Appendix

A. Spatial and Temporal Sensitivity Studies

To assess the grid sensitivity, in total 4 grids are employed with increasing number of cells on the chord and the edges being 16×3, 31×5, 61×9, 121×17, and 241×33. For *Re* = 100, time histories of lift coefficient on the 31×5, 61×9, and 121×17 are compared in Fig. A1 using 480 time steps per motion period for rigid flat plates at k = 0.33. The time histories on the 61×9 and the 121×17 are close and the mean and the RMS lift converges. Hence, all computations presented are performed on the 61×9 grid, see also Table A1. To investigate temporal sensitivity, three time steps were used: T/dt = 240, 480, and 960 on the 61×9 grid. Figure A2 shows that the computations using T/dt = 480 is sufficient to obtain grid and time step independent solution.

At *Re* = 1000 finer mesh is required to capture smaller the viscous effects. Grid refinement study summarized in Table A2 for case 6 (Π_1 = 1.5, k = 1.125) shows that the 121×17 mesh is sufficient.

B. Details of the Surrogate Models

The list of the training points used to populate the design space is summarized in Table B1. The design variables are Π_1 and *k*. The surrogate models are obtained by employing the weighted average surrogates (WAS) to minimize the risk of generating surrogates that fit the training data well but perform less in other regions. The weighted average surrogates (WAS) use constant weights, meaning that a certain surrogate will have the same importance throughout the design space. The Polynomial Response Surface (PRS) [55], Kriging (KRG) [56], and Support Vector Regression (SVR) [57] are used for the individual surrogates, after which each surrogate is weighted in correlation to the RMS PRESS [21]. For each surrogate models different kernel functions and input parameters are systematically assessed and the combination resulting in the lowest RMS PRESS was selected. Specifically, for the PRS the degree of the polynomial surface was selected from 0, 1, or 2 and for the KRG the correlation functions (Cubic, Exponential, Gaussian, Linear, Spherical, Spline), polynomial degrees (0, 1, 2), and the correlation function parameter were considered. For the SRG, we considered different correlation functions (Gaussian, Exponential, Linear Spline, Anova Spline), capacity parameter, the soft-margin loss parameter, and the variance parameters when the Guassian or the Exponential correlation functions were used. Table B2 shows the RMS PRESS values as predicted by the individual surrogate models for $<C_L>$, $<C_P>$, and η and the surrogates that are weighted in the WAS.

To assess the performance of the resulting surrogates, objective functions are computed at independent testing points, chosen arbitrarily in the region of high lift and high efficiency: (Π_1, k) = (1.6, 1.8) and (0.3, 0.75), for the testing points 1 and 2, respectively. The errors normalized by the range of the objective functions are listed in Table B2.

References

[1] A.A. Biewener, *Animal Locomotion*. New York: Oxford University Press, 2003.

[2] W. Shyy, Y. Lian, J. Tang, D. Viieru, and H. Liu, *Aerodynamics of Low Reynolds Number Flyers*.: Cambridge University Press, 2008.

[3] A. Azuma, *The Biokinetics of Flying and Swimming*, 2nd ed. Virginia: AIAA, Inc., 2006.

[4] T. Weis-Fogh, "Quick Estimates of Flight Fitness in Hovering Animals, including Novel Mechanism for Lift

Production," *Journal of Experimental Biology*, vol. 59, pp. 169 - 230, 1973.

[5] C.P. Ellington, C. van den Berg, A.P. Willmott, and A.L.R. Thomas, "Leading-edge Vortices in Insect Flight," *Nature*, vol. 384, pp. 626 - 630, 1996.

[6] M.H., Lehmann, F.-O., Sane, S.P. Dickinson, "Wing Rotation and the Aerodynamic Basis of Insect Flight," *Science*, vol. 284, no. 5422, pp. 1954-1960.

[7] G.K., Nudds, R.L., Thomas, A.L.R. Taylor, "Flying and Swimming Animals Cruise at a Strouhal Number Tuned for High Power Efficiency," *Nature*, vol. 425, pp. 707-711, 2003.

[8] M.S. Triantafyllou, G.S. Triantafyllou, and D.K.P. Yue, "Hydrodynamics of Fishlike Swimming," *Annual Review of Fluid Mechanics*, vol. 32, pp. 33 - 53, 2000.

[9] S. A. Combes and T. L. Daniel, "Flexural Stiffness in Insect Wings I. Scaling and the Influence of Wing Venation," *J. Exp. Biol.*, vol. 206, no. 17, pp. 2979 - 2987, 2003.

[10] F.E. Fish and G.V. Lauder, "Passive and Active Flow Control by Swimming Fishes and Mammals," *Annual Review of Fluid Mechanics*, vol. 38, pp. 193-224, 2006.

[11] B.C. Jayne, A. Lozada, and G.V. Lauder, "Function of the Dorsal Fin in Bluegill Sunfish: Motor Patterns during Four Locomotor Behaviors," *Journal of Morphology*, vol. 228, pp. 307–326, 1996.

[12] W. Shyy, H. Aono, S. K. Chimakurthi, P. Trizila, C.-K. Kang, C. E. S. Cesnik, and H. Liu, "Recent Progress in Flapping Wing Aerodynamics and Aeroelasticity," *Progress in Aerospace Sciences*, vol. 46, no. 7, pp. 284-327, 2010.

[13] S. Ramananarivo, R. Godoy-Diana, and B. Thiria, "Rather than Resonance, Flapping Wing Flyers May Play on Aerodynamics to Improve Performance," *Proceedings of the National Academy of Sciences*, vol. 108, no. 15, pp. 5964 - 5969, 2011.

[14] C. Kang, H. Aono, C.E.S. Cesnik, and W. Shyy, "Effects of Flexibility on the Aerodynamic Performance of Flapping Wings," *Journal of Fluid Mechanics*, vol. 689, pp. 32 - 74, 2011.

[15] W. Shyy, M. Berg, and D. Ljungqvist, "Flapping and Flexible Wings for Biological and Micro Air Vehicles," *Progress in Aerospace Sciences*, vol. 35, pp. 155 - 205, 1999.

[16] B. Thiria and R. Godoy-Diana, "How Wing Compliance Drives the Efficiency of Self-propelled Flapping Flyers," *Physical Review E*, vol. 82, no. 1, p. 015303, 2010.

[17] S. Michelin and S.G. Llewellyn Smith, "Resonance and Propulsion Performance of a Heaving Flexible Wing," *Physics of Fluids*, vol. 21, p. 071902, 2009.

[18] J. Zhang, N.-S. Liu, and X.-Y. Lu, "Locomotion of a Passively Flapping Flat Plate," *Journal of Fluid Mechanics*, vol. 659, pp. 43 - 68, 2010.

[19] M. Vanella, T. Fitzgerald, S. Preidikman, E. Balaras, and B. Balachandran, "Influence of Flexibility on the Aerodynamic Performance of a Hovering Wing," *Journal of Experimental Biology*, vol. 212, pp. 95 - 105, 2009.

[20] H. Masoud and A. Alexeev, "Resonance of Flexible Flapping Wings at Low Reynolds Number," *Physical Review E*, vol. 81, p. 056304, 2010.

[21] P. Trizila, C.-K. Kang, H. Aono, M. Visbal, and W. Shyy, "Low-Reynolds-number Aerodynamics of a Flapping Rigid Flat Plate," *AIAA Journal*, vol. 49, no. 4, pp. 806-823, 2011.

[22] A.R. Ennos, "The Inertial Cause Of Wing Rotation in Diptera," *Journal of Experimental Biology*, vol. 140, pp. 161 - 169, 1988.

[23] J.D. Eldredge, J. Toomey, and A. Medina, "The Roles of Chord-wise Flexibility in a Flapping Wing," *Journal of Fluid Mechanics*, vol. 659, pp. 94 - 115, 2010.

[24] D. Ishihara, T. Horie, and M. Denda, "A Two-dimensional Computational Study on the Fluid–Structure Interaction Cause of Wing Pitch Changes in Dipteran Flapping Flight," *Journal of Experimental Biology*, vol. 212, pp. 1-10, 2009.

[25] S. Spagnolie, L. Moret, M.J. Shelley, and J. Zhang, "Surprising Behaviors in Flapping Locomotion with Passive Pitching," *Physics of Fluids*, vol. 22, p. 041903, 2010.

[26] N. Vandenberghe, J. Zhang, and S. Childress, "Symmetry Breaking Leads to Forward Flapping Flight," *Journal of Fluid Mechanics*, vol. 506, pp. 147 - 155, 2004.

[27] A. Magnan, *Le Vol des Insectes*. Paris, France: Hermann et Cie, 1934.

[28] D. Campos, L.S. Ukeiley, and L.P. Bernal, "Flow Around Flapping Flexible Flat Plate Wings," in *50th AIAA Aerospace Sciences Meeting including the New Horizons Forum and Aerospace Exposition, Nashville, Tennessee*, 9 - 12 Jan 2012.

[29] C.E.S. Cesnik, L.P. Bernal, R. Vandenheede, D. Kumar, and C. Morrison, "Influence of Isotropic and Anisotropic Flexibility on the Performance of Pitching and Plunging Wings in Hover," in *50th AIAA Aerospace Sciences Meeting including the New Horizons Forum and Aerospace Exposition, Nashville, Tennessee* , 9 - 12 Jan 2012.

[30] L. Zhao, Huang, Q. , X. Deng, and S.P. Sane, "Aerodynamic Effects of Flexibility in Flapping Wings," *Journal of the Royal Society Interface*, vol. 7, pp. 485 - 497, 2010.

[31] J. A. Wright and R. W Smith, "An Edge-based Method for the Incompressible Navier-Stokes Equations on Polygonal Meshes," *Journal of Computational Physics*, vol. 169, pp. 24 - 43, 2001.

[32] R. W. Smith and J. A. Wright, "An Implicit Edge-based ALE Method for the Incompressible Navier-Stokes Equations," *International Journal of Numerical Methods in Fluids*, vol. 43, pp. 253 - 279, 2003.

[33] R. Kamakoti, S. Thakur, J. Wright, and W. Shyy, "Validation of a New Parallel All-Speed Cfd Code in a Rule-based Framework for Multidisciplinary Applications," in *36th AIAA Fluid Dynamics Conference and Exhibit, San Francisco, California*, June 5-8, 2006, AIAA-2006-3063.

[34] S. Balay, W. D. Gropp, L. C. McInnes, and B. F. Smith, "Efficient Management of Parallelism in Object Oriented Numerical Software Libraries," in *Modern Software Tools in Scientific Computing*, 1997, pp. 163-202.

[35] S. Balay, J. Brown, K. Buschelman, V. Eijkhout, W. D. Gropp, D. Kaushik, M. G. Knepley, L. C. McInnes, B. F. Smith, and H. Zhang, "PETSc Users Manual," Argonne National Laboratory, 2010.

[36] S. Balay, J. Brown, K. Buschelman, W. D. Gropp, D. Kaushik, M. G. Knepley, L. C. McInnes, B. F. Smith, and H. Zhang. (2011) PETSc Web page. [Online]. http://www.mcs.anl.gov/petsc

[37] R. Falgout and U. Yang, "hypre: A Library of High Performance Preconditioners," in *Computational Science — ICCS 2002*, Peter Sloot, Alfons Hoekstra, C. Tan, and Jack Dongarra, Eds.: Springer Berlin / Heidelberg, 2002, pp. 632-641.

[38] E. A. Luke and T. George, "Loci: a Rule-based Framework for Parallel Multi-disciplinary Simulation Synthesis," *Journal of Functional Programming*, vol. 15, no. 03, pp. 477 - 502, 2005.

[39] P.D. Thomas and C. K. Lombard, "Geometric Conservation Law and its Application to Flow Computations on Moving Grids," *AIAA Journal*, vol. 17, no. 10, pp. 1030 - 1037, 1979.

[40] R. Kamakoti and W. Shyy, "Evaluation of Geometric Conservation Law using Pressure-based Fluid Solver and Moving Grid Technique," *International Journal of Heat and Fluid Flow*, vol. 14, no. 7, pp. 851 - 865, 2004.

[41] A. de Boer, M. S. van, and H. Bijl, "Mesh Deformation Based on Radial Basis Function Interpolation," *Computers & Structures*, vol. 85, no. 11-14, pp. 784 - 795, 2007.

[42] N. Queipo, R. T. Haftka, W. Shyy, T. Goel, R. Vaidyanathan, and P.K. Tucker, "Surrogate-Based Analysis and Optimization," *Progress in Aerospace Sciences*, vol. 41, no. 1, pp. 1 – 25, 2005.

[43] W. Shyy, N. Papila, R. Vaidyanathan, and P. K. Tucker, "Global Design Optimization for Aerodynamics and Rocket Propulsion Optimization," *Progress in Aerospace Sciences*, vol. 37, no. 1, pp. 59 - 118, 2001.

[44] S.P. Sane and M.H. Dickinson, "The Control of Flight Force by a Flapping Wing: Lift and Draft," *Journal of Experimental Biology*, vol. 204, pp. 2607 – 2626, 2001.

[45] H Hu, L. Clemens, and H. Igarashi, "An Experimental Study of the Unsteady Vortex Structures in the Wake of a Root-fixed Flapping Wing," *Experiments in Fluids*, vol. 51, pp. 347 - 359, 2011.

[46] N. Vandenberghe, S. Childress, and J. Zhang, "On Unidirectional Flight of a Free Flapping Wing," *Physics of Fluids*, vol. 18, p. 014102, 2006.

[47] J.M. Birch, W.B. Dickson, and M.H. Dickinson, "Force Production and Flow Structure of the Leading Edge Vortex on Flapping Wings at High and Low Reynolds Numbers," *Journal of Experimental Biology*, vol. 207, pp. 1063 - 1072, 2004.

[48] W. Shyy and H. Liu, "Flapping Wings and Aerodynamic Lift: The Role of Leading-Edge Vortices," *AIAA Journal*, vol. 45, no. 12, pp. 2817 - 2819, 2007.

[49] Z.J. Wang, "The Role of Drag in Insect Hovering," *Journal of Experimental Biology*, vol. 207, pp. 4147 - 4155, 2004.

[50] G. Du and M. Sun, "Effects of Wing Deformation on Aerodynamic Forces in Hovering Hoverflies," *Journal of Experimental Biology*, vol. 213, pp. 2273 - 2283, 2010.

[51] X.L. Mou, Y.P. Liu, and M. Sun, "Wing Motion Measurement and Aerodynamics of Hovering True Hoverflies," *Journal of Experimental Biology*, vol. 214, pp. 2832 - 2844, 2011.

[52] P Freymuth, "Thrust Generation by an Airfoil in Hover Modes," *Experiments in Fluids*, vol. 9, pp. 17 - 24, 1990.

[53] F.-O. Lehmann, Gorb. S., N. Nasir, and P. Schützner, "Elastic Deformation and Energy Loss of Flapping Fly Wings," *Journal of Experimental Biology*, vol. 214, pp. 2949 - 2961, 2011.

[54] S. A. Combes and T. L. Daniel, "Into Thin Air: Contributions of Aerodynamic and Inertial-elastic Forces to Wing Bending in the Hawkmoth Manduca Sexta," *Journal of Experimental Biology*, vol. 206, pp. 2999 - 3006, 2003.

[55] R. H. Myers and D. C. Montgomery, *Response Surface Methodology: Process and Product Optimization Using Designed Experiments*. Hoboken, NJ: Wiley, 2002.

[56] J. Sacks, S. B. Schiller, and W. J. Welch, "Design for Computer Experiments," *Technometrics*, vol. 31, no. 1, pp. 41 - 47, 1989.

[57] A.I.J. Forrester and A.J. Keane, "Recent Advances in Surrogate-based Optimization," *Progress in Aerospace Sciences*, vol. 45, pp. 50 - 79, 2009.

Figures and Tables

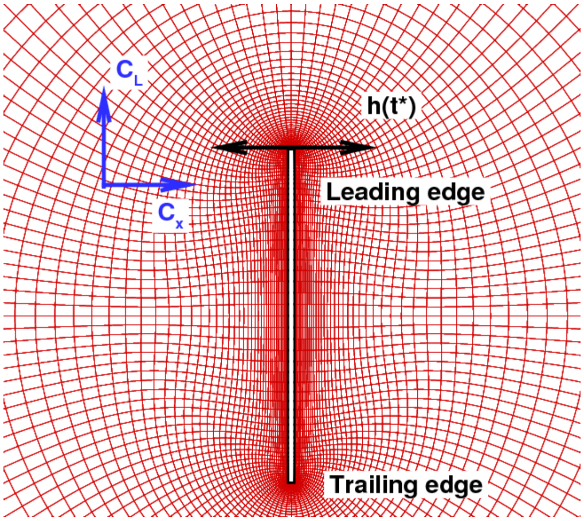

(a) Definitions of various directions.

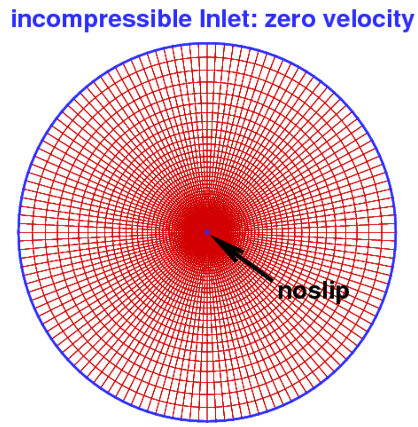

(b) Imposed boundary conditions.

Figure 1. Computational domain for the fluid flow, flat plate geometry, and the directions of lift C_L and plunging motion $h^*(t^*)$. A sinusoidal plunging motion given by Eq. (5) is imposed at the leading edge and a free boundary condition is applied at the trailing edge of the flat plate. The boundary conditions for the fluid flow are the incompressible inlet with zero velocity at the outer boundary of the computational domain and noslip on the flat plate surface.

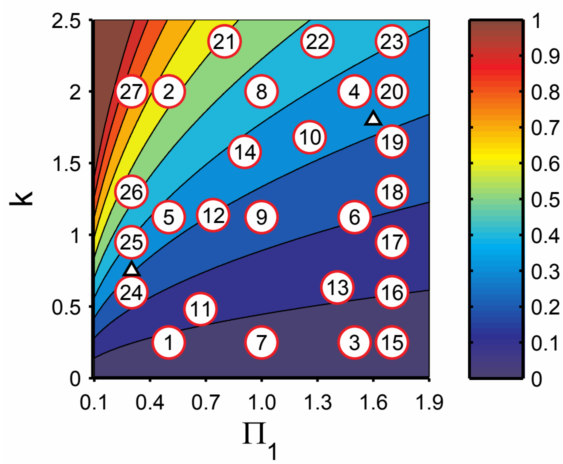

Figure 2. Design of experiment for the design variables Π_1 and k. The contour represents the frequency ratio, f/f_1. The numbers indicate the case number as listed in Table B1. The triangles indicate the locations of the testing points.

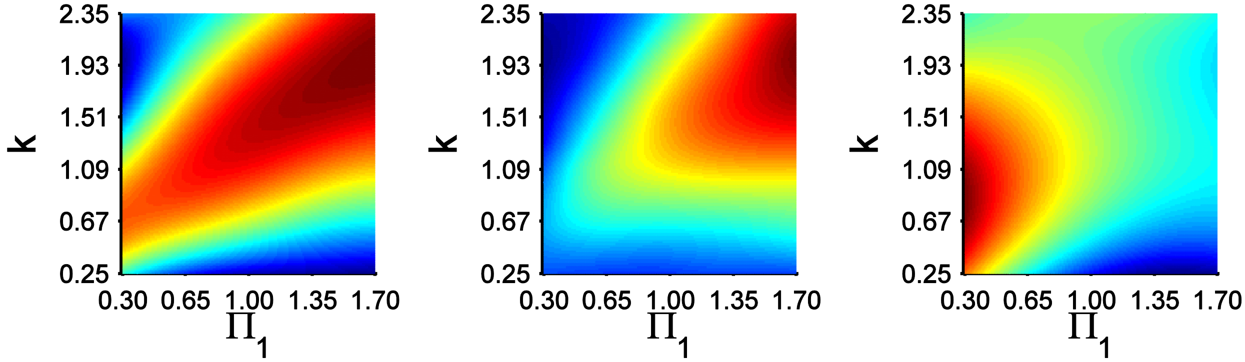

(a) $<C_L>$, *Re* = 100 (b) $<C_P>$, *Re* = 100 (c) η, *Re* = 100

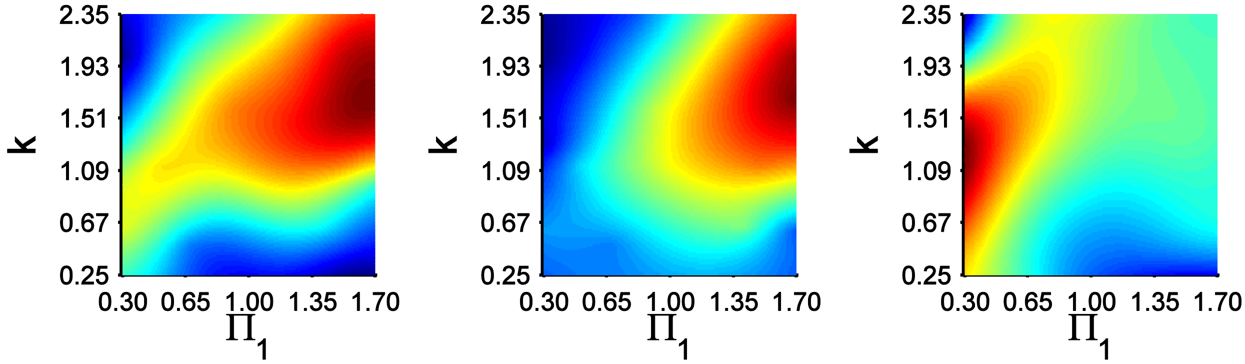

(d) $<C_L>$, *Re* = 1000 (e) $<C_P>$, *Re* = 1000 (f) η, *Re* = 1000

Figure 3. Surrogate model responses for (a,d) lift, (b,e) power input, and (c,f) efficiency for *Re* = 100 (top row) and 1000 (bottom). Red and blue regions indicate maximum and minimum contour levels, (a,d): 0 to 2.5; (b,e): 0 to 5; (c,f): 0 to 1, respectively. There are 20 contour levels for each subfigure.

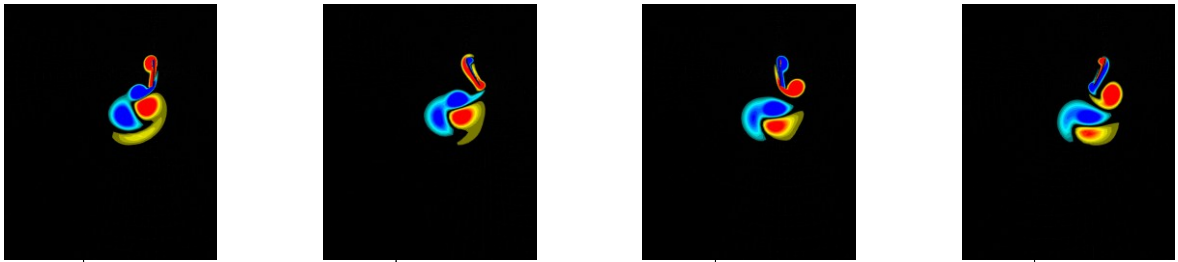

$t^* = 0.0$ $t^* = 0.25$ $t^* = 0.50$ $t^* = 0.75$

(a) Vorticity field. Red and blue regions indicate positive and negative vorticity, respectively; the magnitude of the vorticity at the outer contour is 4 and the contour interval is 0.4. The contour levels -0.4 and 0.4 are removed and 0 indicated by black for better contrast.

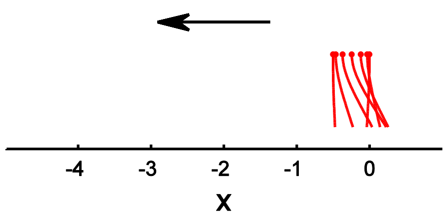

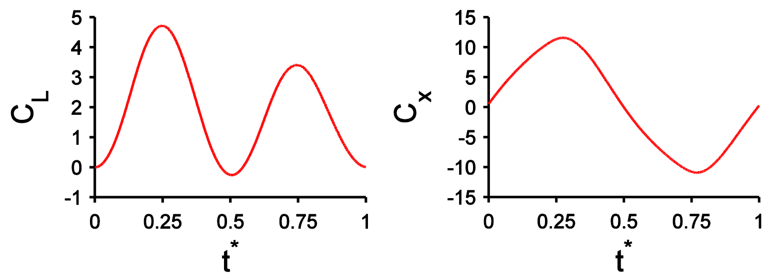

(b) Seven snapshots of the flat plate shape during the backward stroke with equal time intervals. The LE is indicated with a circle at $x = 0$ at $t^* = 0.0$.

(c) Time histories of forces

Figure 4. Maximum lift case ($\Pi_1 = 1.7$, $k = 2$). $\langle C_L \rangle = 1.78$, $\eta = 0.34$.

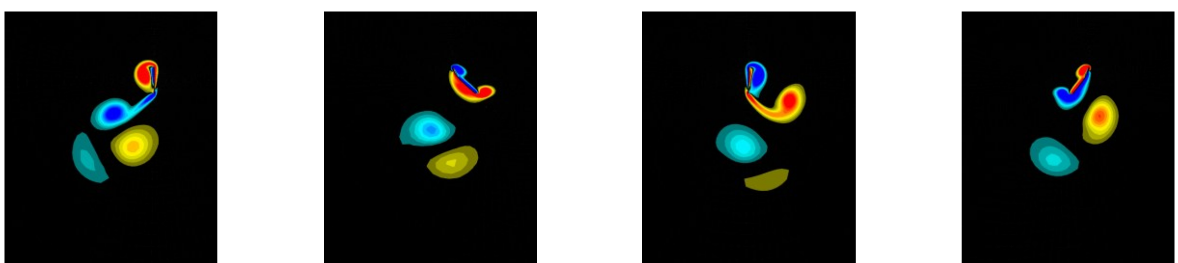

$t^* = 0.0$ $t^* = 0.25$ $t^* = 0.50$ $t^* = 0.75$

(a) Vorticity field.

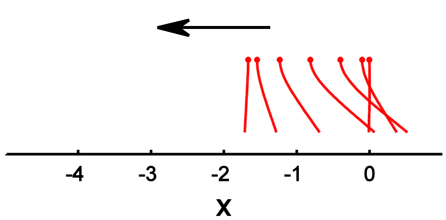

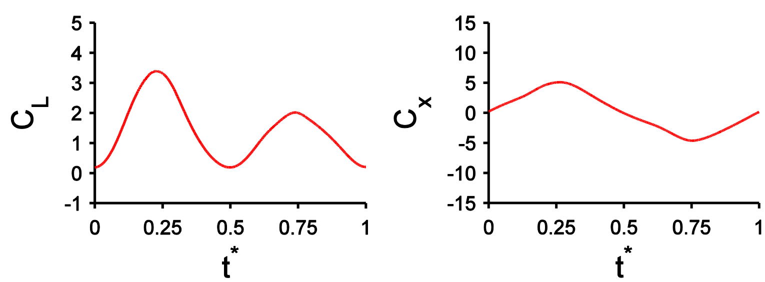

(b) Flat plate shapes.

(c) Time histories of forces.

Figure 5. Optimal efficiency case ($\Pi_1 = 0.3$, $k = 0.6$). $\langle C_L \rangle = 1.45$, $\eta = 0.66$. The format for each subfigure is that of Fig. 4.

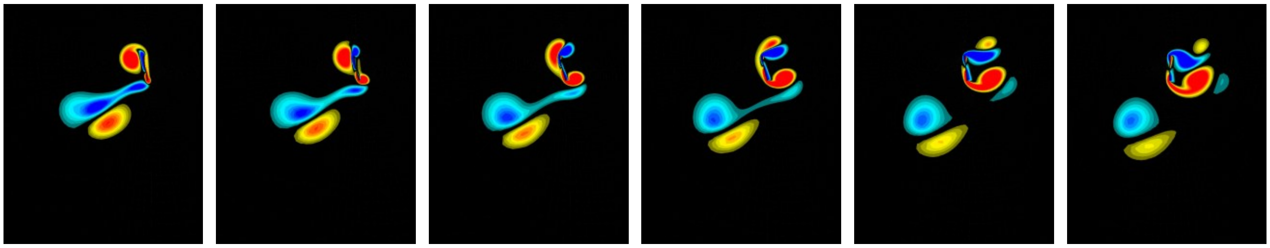

(a) (1.7, 0.6)

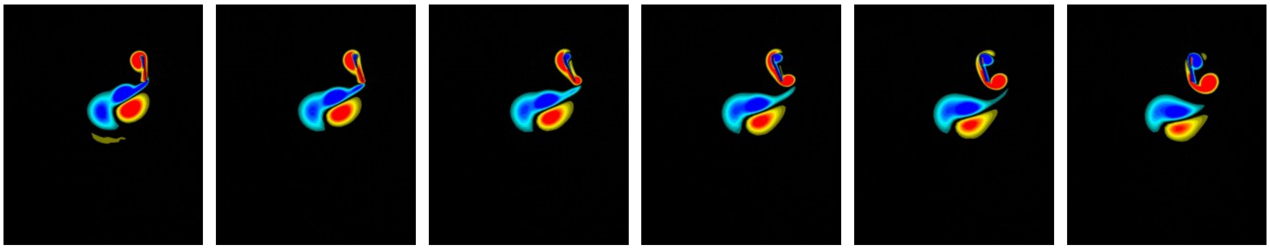

(b) (1.7, 1.3)

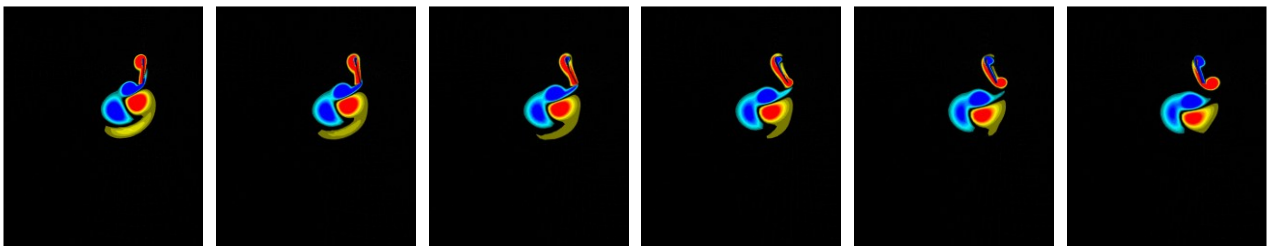

(c) (1.7, 2.0)

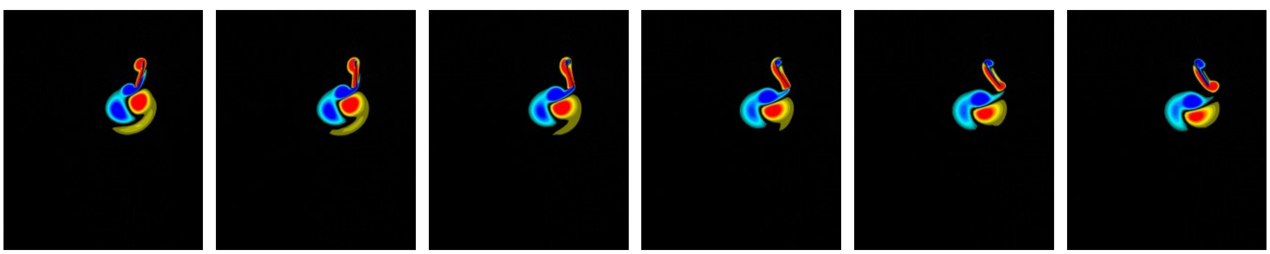

(d) (1.0, 2.0)

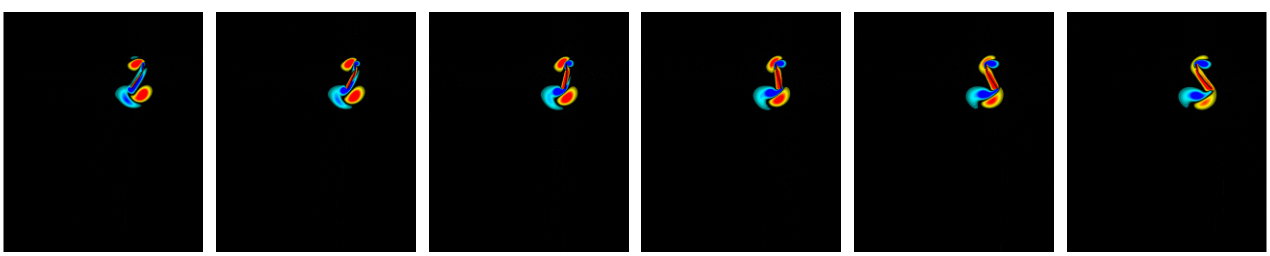

(e) (0.3, 2.0)

$t^* = 0.0$ $t^* = 0.083$ $t^* = 0.167$ $t^* = 0.250$ $t^* = 0.333$ $t^* = 0.417$

Figure 6. Vorticity contours at several time instants during a backstroke. The values in the parentheses correspond to (Π_1, *k*). The description of the vorticity contours are in Fig. 4.

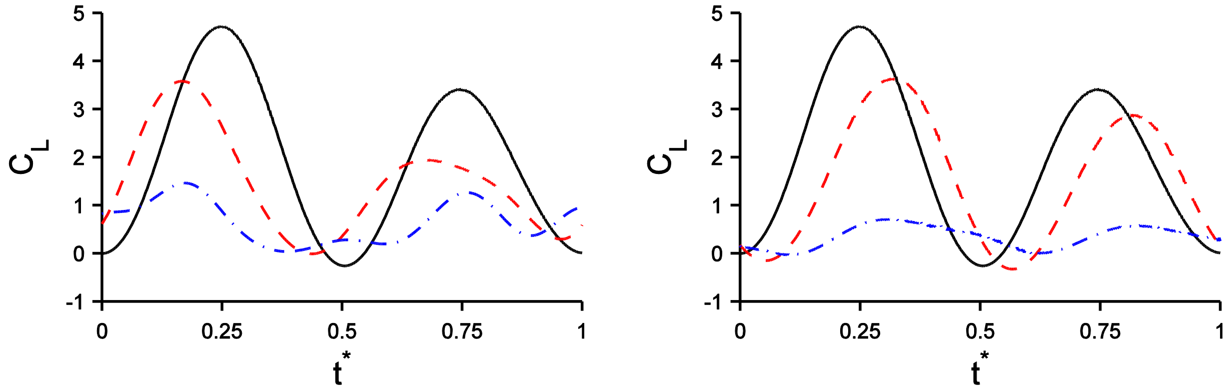

(a) k effect at $\Pi_1 = 1.7$: $k = 2.0$ (—), 1.3 (– –), 0.6 (–·–·) (b) Π_1 effect at $k = 2.0$: $\Pi_1 = 1.7$ (—), 1.0 (– –), 0.3 (–·–·)

Figure 7. Time history of lift to illustrate k and Π_1 effects with respect to the maximum lift case ($\Pi_1 = 1.7$, $k = 2.0$)

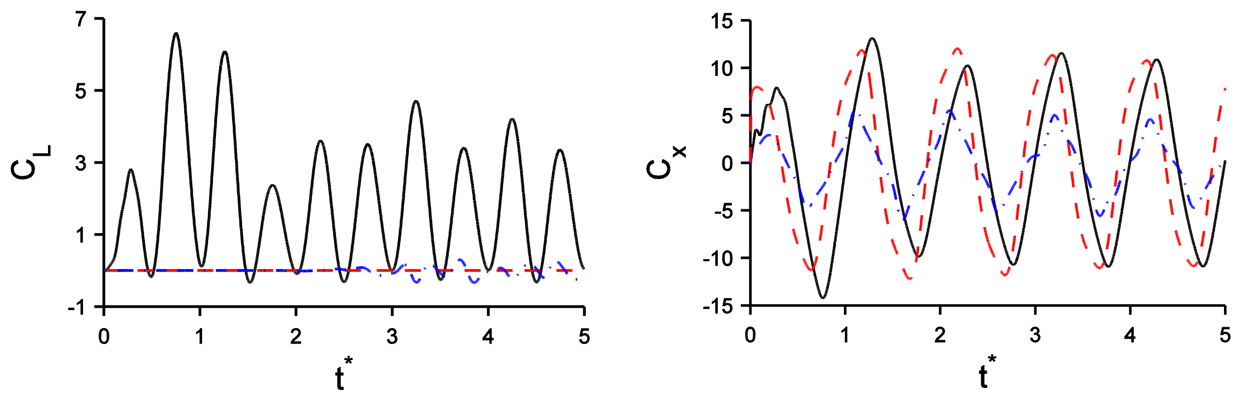

(a) Time history of lift (b) Time history of lateral force

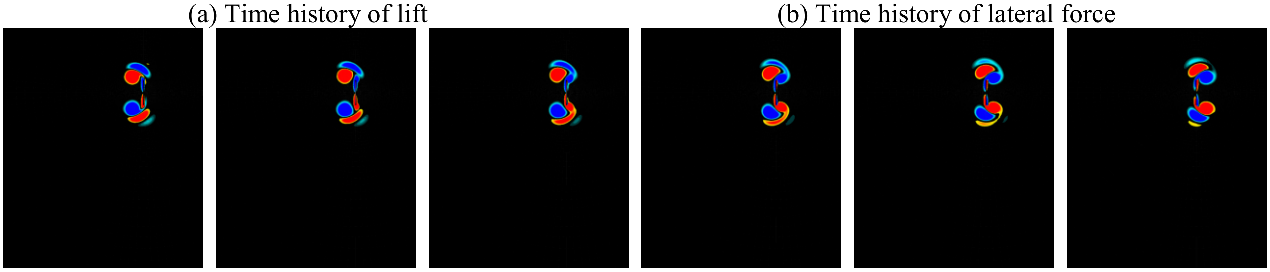

(c) rigid; $k = 2.0$

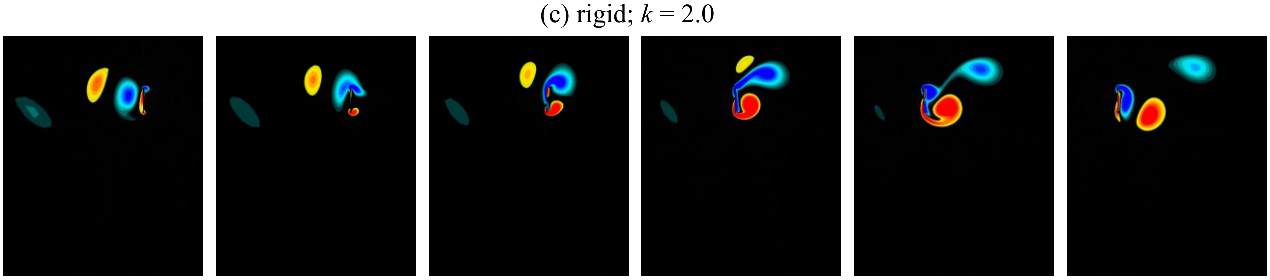

(d) rigid; $k = 0.25$

$t^* = 0.0$ $t^* = 0.083$ $t^* = 0.167$ $t^* = 0.250$ $t^* = 0.333$ $t^* = 0.417$

Figure 8. Time history of forces and vorticity contours of a hovering rigid flat plate: (a,b): $\Pi_1 = 1.7$, $k = 2.0$ (—), rigid $k = 2.0$ (– –), rigid $k = 0.25$ (–·–·), t^* from the first cycle. (c,d): The description of the vorticity contours are in Fig. 4.

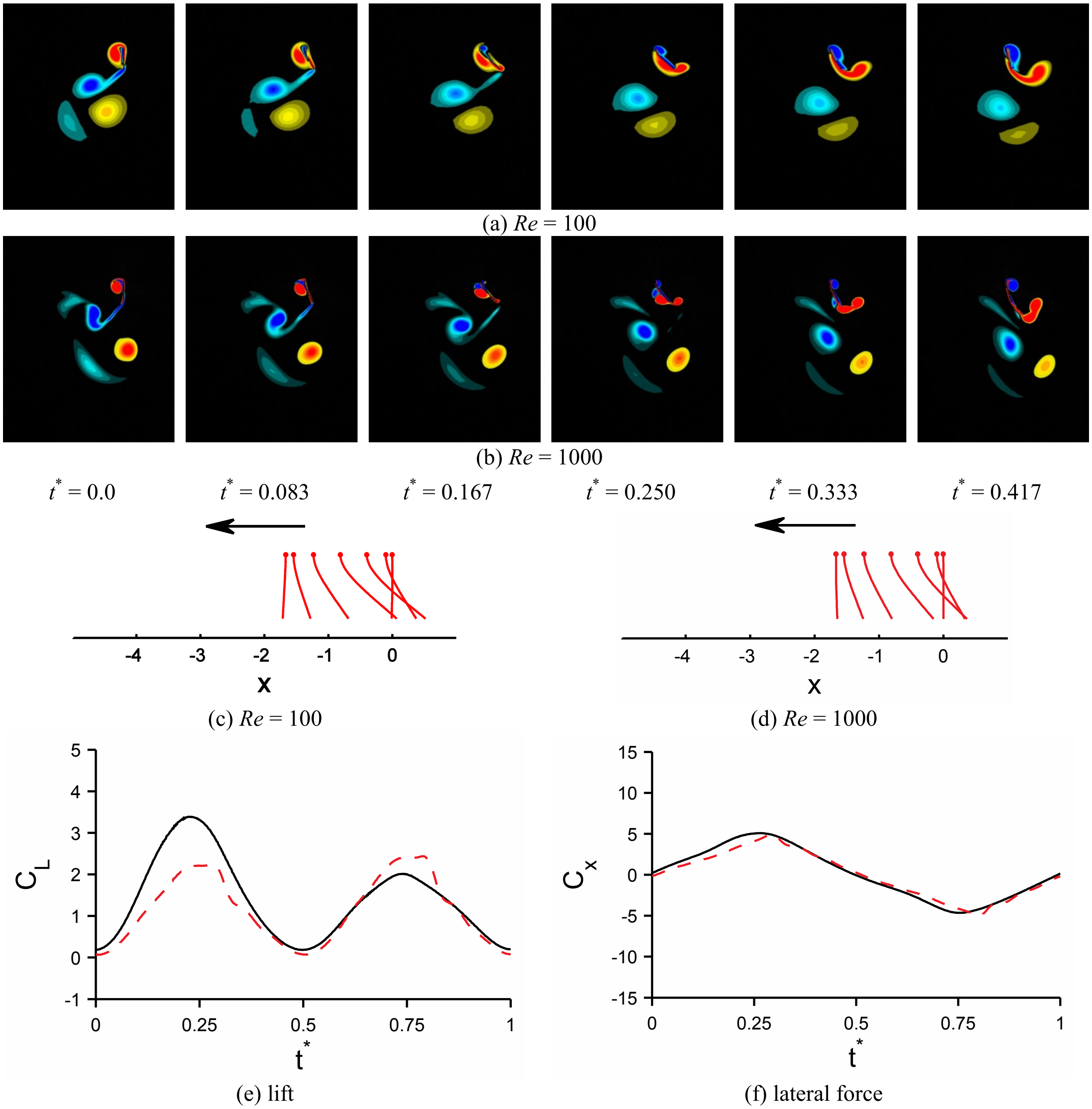

Figure 9. Reynolds number effects for the the case (Π_1 = 0.3, *k* = 0.6) with the highest efficiency at *Re* = 100 (a,b) Vorticity contours; (c,d): Flat plate shapes; (e,f): Time history of forces; *Re* = 100 (—), 1000 (--).The description of the vorticity contours and the flat plate shapes are in Fig. 4

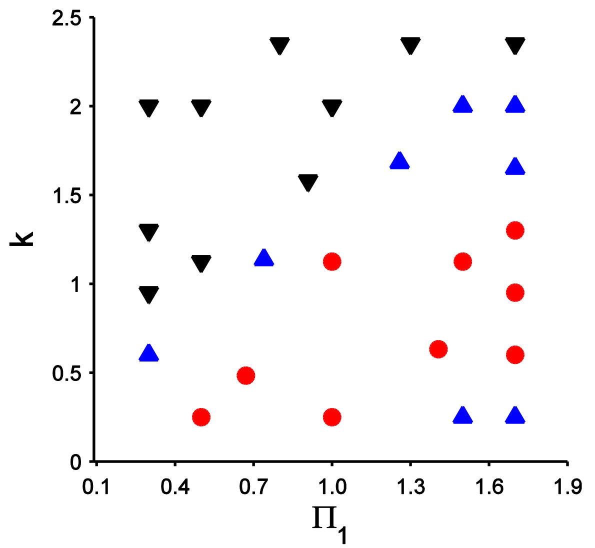

(a) distribution of advanced, synchronized, and delayed rotation modes in the (Π_1, k) design space.

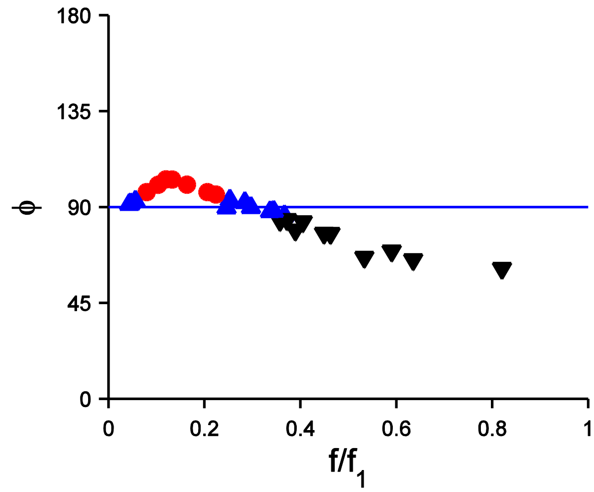

(b) phase lag vs. frequency ratio

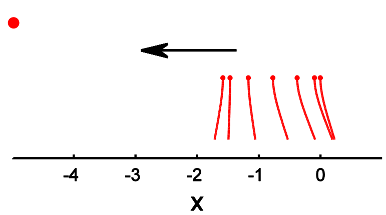

(c) advanced rotation (1.4, 0.63)

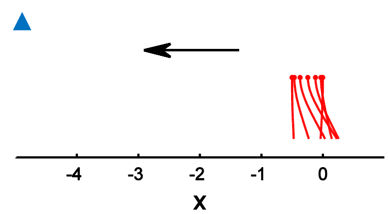

(d) synchronized rotation (1.7, 2.0)

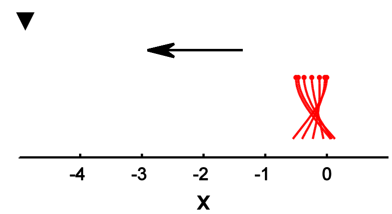

(e) delayed rotation (0.3, 2.0)

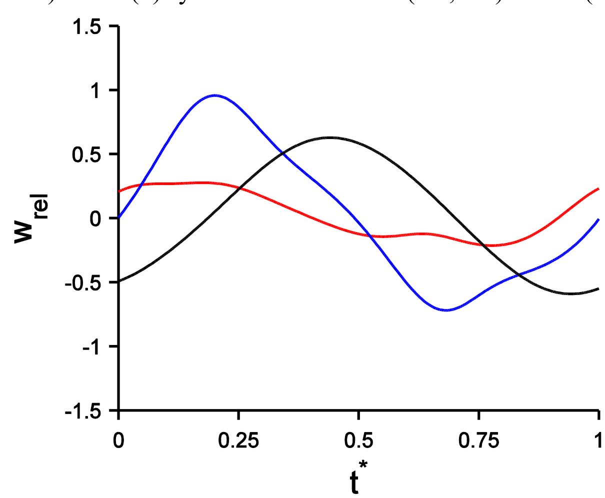

(f) Time history of relative tip deformation for an advanced rotation (—,1.4, 0.63) $\langle C_L \rangle = 0.84$, synchronized rotation (—, 1.7, 2.0) $\langle C_L \rangle = 1.45$, and delayed rotation (—, 0.3, 2.0) $\langle C_L \rangle = 0.32$ case.

Figure 10. (a): Distribution of the three hovering modes in the design space. ●: advanced rotation, ▲: synchronized rotation, ▼: delayed rotation; (b) Relation between the phase lag, φ, between the TE and the LE at the stroke ends for the cases considered at *Re* = 100; (c,d,e): Shapes of the flat plate during the backward stroke at seven equal time intervals. (f) Time history of tip displacement relative to the LE of the flat plate for the three rotation modes; The values in the parentheses indicate Π_1 and *k*, respectively.

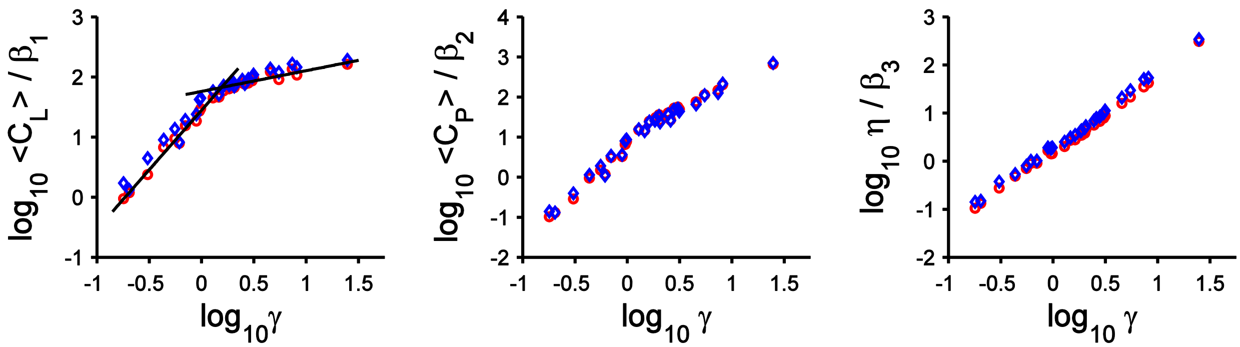

(a) $\langle C_L \rangle$ (b) $\langle C_P \rangle$ (c) η

Figure 11. Normalized aerodynamic performance against γ; o: *Re* = 100, ◊: *Re* = 1000

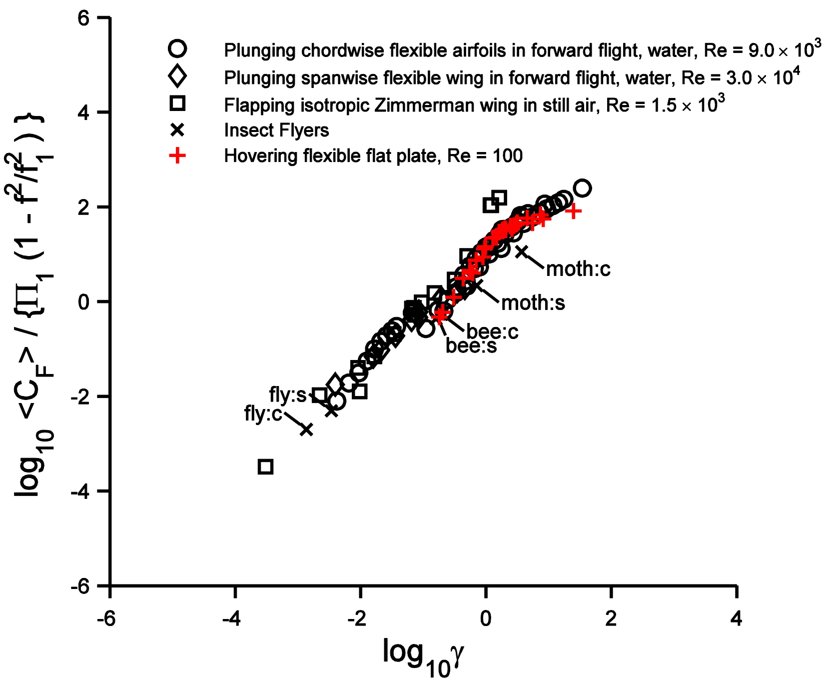

Figure 12. Normalized time-averaged force coefficients as function of γ following the revised scaling Eq. (9). The data for the chordwise, spanwise, isotropic wings, and insects are from our previous study [14].

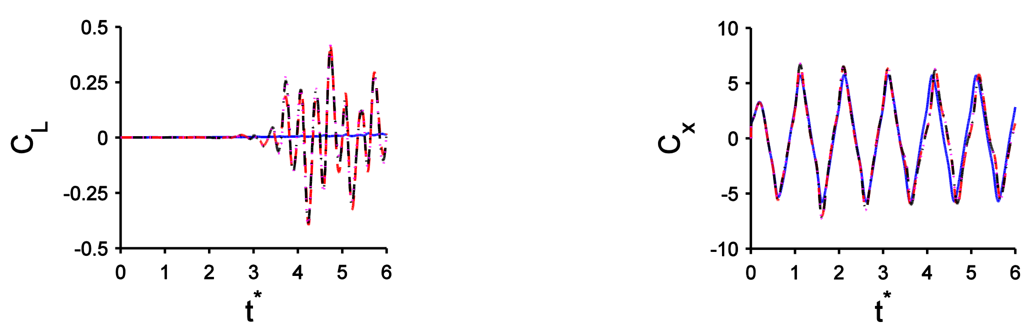

(a) lift (b) lateral

Figure A1. Grid sensitivity of a plunging rigid flat plate at *Re* = 100 with *k* = 0.33. 16×3 (—), 31×5 (– –), 61×9 (–·–·), 121×17 (·····). *T*/d*t* = 480 is used.

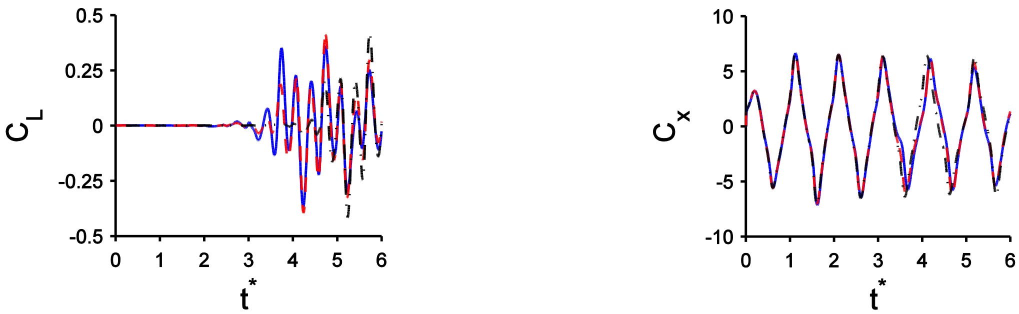

(a) lift (b) lateral

Figure A2. Time sensitivity of a plunging rigid flat plate at *Re* = 100 with *k* = 0.33 on the intermediate grid: *T*/d*t* = 240 (—), *T*/d*t* = 480 (– –), *T*/d*t* = 960 (–·–·).

Table 1. Non-dimensional parameter range considered in this study

Non-dimensional parameters	Parameter	Design Variable	
Re	100		
ρ^*	2×10^3		
h_s^*	0.02		
k (h_a)		0.25 - 2	(0.25 – 2)
Π_1 (E)		0.5 - 1.5	(7.5×10^5- 2.25×10^6)

Table 2. Swimming vs. Flying

	Swimming	Flying
γ	$\sim h_a^*/\{\rho^* h_s^* (f_1^2/f^2-1)\}$	$\sim h_a^*/(f_1^2/f^2-1)$
Deforming force	added mass	inertial force
Optimal k for cruise	0.5 – 0.6 [3]	0.25 [2]

Table A1. Spatial and temporal sensitivity for *Re* = 100 rigid case at k = 0.33

		$<C_L>$	Relative error	RMS error
spatial	31×5	0.0022	2.9	0.035
	61×9	0.0082	0.75	0.012
	121×17	0.010	baseline	
temporal	240	0.021	15	0.087
	480	0.0082	5.6	0.044
	960	0.00090	baseline	

Table A2. Spatial sensitivity for *Re* = 1000 for at Π_1 = 1.5, *k* = 1.125

		$<C_L>$	Relative error	RMS error
Spatial	61×9	2.18	1.4	0.82
	121×17	1.93	0.7	0.32
	241×33	1.92	baseline	

Table B1. List of training points in the design space and the objective functions. Π_1 and k are the design variables and $\langle C_L \rangle$, $\langle C_P \rangle$, and η are the objective functions.

Case	Π_1	k	Re = 100			Re = 1000		
			$\langle C_L \rangle$	$\langle C_P \rangle$	η	$\langle C_L \rangle$	$\langle C_P \rangle$	η
1	0.5	0.25	0.64	1.69	0.38	0.98	1.97	0.50
2	0.5	2	0.65	1.36	0.48	0.86	1.41	0.61
3	1.5	0.25	0.29	1.70	0.17	0.38	2.07	0.18
4	1.5	2	1.73	4.80	0.36	2.19	4.63	0.47
5	0.5	1.125	1.52	2.74	0.55	1.63	2.40	0.68
6	1.5	1.125	1.40	3.92	0.36	1.84	4.22	0.44
7	1.0	0.25	0.39	1.66	0.23	0.57	2.20	0.26
8	1.0	2	1.40	3.30	0.42	1.60	2.99	0.53
9	1.0	1.125	1.56	3.71	0.42	1.74	3.61	0.48
10	1.26	1.19	1.71	4.43	0.39	2.03	4.23	0.48
11	0.67	0.48	1.02	2.22	0.46	0.82	1.99	0.41
12	0.74	1.14	1.61	3.39	0.48	1.63	3.02	0.54
13	1.41	0.63	0.84	2.64	0.32	1.08	3.06	0.35
14	0.91	1.58	1.61	3.65	0.44	1.83	3.35	0.55
15	1.7	0.25	0.26	1.73	0.15	0.33	1.84	0.18
16	1.7	0.60	0.77	2.71	0.28	0.71	1.78	0.40
17	1.7	0.95	1.10	3.44	0.32	1.15	3.31	0.35
18	1.7	1.30	1.50	4.37	0.34	2.04	4.65	0.44
19	1.7	1.65	1.72	4.99	0.34	2.36	5.30	0.44
20	1.7	2.00	1.78	5.19	0.34	2.28	5.16	0.44
21	0.8	2.35	0.82	1.88	0.43	1.04	1.74	0.59
22	1.3	2.35	1.40	3.65	0.38	1.64	3.40	0.48
23	1.7	2.35	1.68	4.89	0.34	2.02	4.55	0.44
24	0.3	0.60	1.45	2.19	0.66	1.51	2.12	0.71
25	0.3	0.95	1.33	2.03	0.65	1.51	1.77	0.85
26	0.3	1.30	0.91	1.44	0.63	1.11	1.22	0.90
27	0.3	2.00	0.32	0.94	0.35	0.36	0.94	0.39

Table B2. Best RMS PRESS values and the relative error at three independent testing points. The surrogate models with the RMS PRESS indicated with bold are used in the WAS construction.

Re		KRG	SVR	PRS	Test Point 1	Test Point 2
100	$\langle C_L \rangle$	0.0830	**0.0748**	0.1294	2.7%	0.2%
	$\langle C_P \rangle$	**0.0417**	**0.0572**	0.0624	0.7%	0.7%
	η	0.1088	**0.0929**	0.1432	1.6%	0.0%
1000	$\langle C_L \rangle$	**0.0884**	**0.0892**	0.1037	4.5%	9.9%
	$\langle C_P \rangle$	0.1394	**0.0735**	0.0961	1.4%	2.7%
	η	**0.1004**	**0.1118**	0.1648	2.7%	6.6%